BAYESIAN EEG SOURCE RECONSTRUCTION USING MARKOV CHAIN MONTE CARLO METHODS

by

Gökçen Yıldız

B.S. in Computer Engineering, Galatasaray University, 2005

Submitted to the Institute of Biomedical Engineering
in partial fulfillment of the requirements
for the degree of
Master of Science
in
Biomedical Engineering

Boğaziçi University
2007

ACKNOWLEDGMENTS

I am deeply indebted to my thesis advisor Prof. Ahmet Ademoğlu whose guidance, stimulating suggestions and encouragement helped me not only during my thesis but in all the time of my master's study.

I am also grateful to Adil Deniz Duru, without him source reconstruction results will only be graphic plots. I hope to keep our collaboration for future studies.

ABSTRACT

BAYESIAN EEG SOURCE RECONSTRUCTION USING MARKOV CHAIN MONTE CARLO METHODS

Electroencephalography (EEG), a non-invasive neuroimaging method measuring neural activity without any metabolic bias, has millisecond scale temporal resolution, the best among available functional imaging techniques with magnetoencephalography(MEG). However, its spatial resolution is severely limited by electrode number used in measurements and head volume conduction effect. Dipole source analysis, EEG forward and inverse problem, aims to compensate for the head volume conduction effect and enhance the spatial resolution of the EEG. Given the known electrical field and head volume conductor properties, the EEG inverse problem estimates the location and magnitude of the brain electrical sources. In this study, EEG inverse problem is formulated using Bayesian inference on a realistic head model. The posterior probability distribution of dipole parameters including the number of active dipoles are sampled by Markov chain Monte Carlo (MCMC) methods. Sampling algorithm is designed by combining Reversible Jump (RJ) which permits trans-dimensional iterations and Parallel Tempering (PT), a heuristic to escape from local optima. Two different approaches to EEG inverse problem, equivalent current dipole (ECD) and distributed imaging are combined in terms of probability. EEG inverse problem is solved with this probabilistic approach using simulated and empirical data. Localization errors are computed. Comparing to multiple signal classification algorithm (MUSIC) and low-resolution electromagnetic tomography (LORETA) methods, this study shows that using MCMC methods with a Bayesian approach is useful for solving the ill-posed EEG inverse problem.

Keywords: EEG, Dipole source localization, Inverse problems, Bayesian inference, MCMC methods.

ÖZET

Beynin elektriksel etkinliğini, diğer metabolik olaylara bağlamaksızın deri üzerinden ölçebilen elektroensefalografi (EEG), manyetoensefalografi (MEG) ile beraber mevcut işlevsel nörogörüntüleme yöntemleri içinde en iyi zamansal çözünürlüğe sahiptir. Uzamsal çözünürlüğü ise ölçümlerde kullanılan elektrot sayısı ve kafa hacminin elektriksel iletimi ile kısıtlıdır. EEG potansiyellerini üreten dipol kaynaklarının analizini içeren ileri ve ters yöndeki problem çözümleri, bu kısıtlamaların EEG'nin uzamsal çözünürlüğü üzerindeki etkilerini kaldırmayı amaçlar. Bu çalışmada, EEG işaretlerini üreten kaynakların beyin dokusu içindeki yerlerini ve genliklerini kestiren ters yönlü problem Bayesçi çıkasama uygulanarak modellendi. Üç boyutlu gerçekçi kafa modelininde belirlenmiş aday dipol kaynaklarının sonsal olasılık dağılımları Markov Zinciri Monte Carlo (MZMC) yöntemleri ile örneklendi. Örnekleme algoritması, farklı boyuttaki çözüm uzayları arası geçiş sağlayan tersinir dallanma (TD) ve yerel en iyilere yakınsamayı azaltan paralel tavlama (PT) yöntemleri kullanılarak oluşturuldu. Ters yönlü probleme iki ayrı yaklaşım olan eşdeğer akım dipolü ve dağıtık görüntüleme olasılıksal bağlamda birleştirildi. Ters yönlü problem bu yaklaşımla, farklı dipol yapılanışlarıyla oluşturulan benzetilmiş anlık EEG verileri ve olaya ilişkin potansiyel verisi üzerinde çözüldü. Yerelleştirme hataları saptandı. Elde edilen sonuçlar, literatürde sıklıkla kullanılan çoklu işaret ayrıştırma yöntemi (MUSIC) ve düşük çözünürlüklü elektromanyetik tomografi (LORETA) yöntemleriyle karşılaştırıldığında, EEG ters yönlü problem çözümünde MZMC yöntemlerinin Bayesçi bir yaklaşımla kullanılmasının oldukça gerçekçi olduğu kanısını güçlendirmiştir.

Anahtar Sözcükler: EEG, Dipol kaynak yerelleştirme, Ters yönlü problem, Bayesçi kestirim, MZMC yöntemleri.

TABLE OF CONTENTS

LIST OF FIGURES

LIST OF TABLES

LIST OF SYMBOLS

B	Inverse filter
B_{LORETA}	Inverse filter of LORETA
E	Objective function
G	Laplacian operator
J_i	Relative strength of the i^{th} dipole source
$\vec{J}_{TIK}$	Current denisity vector found by TIK regularization
K	Lead field matrix
$K^{\dagger}$	Pseudo inverse of K
$\vec{m}$	Dipole moment vector
M	Dipole magnitude
N	Number of active dipoles
N_e	Number of electrodes
N_v	Number of voxels
q^{ind}	Proposal distribution for dipole number
q^{par}	Proposal distribution for dipole parameters
$\vec{r_e}$	Estimated dipole location vector
$\vec{r_o}$	Original dipole location vector
$\vec{r}$	Dipole location vector
T	Temperature
$\vec{V}$	Scalp potentials
X	Design matrix
Y	Observed pixel values
α	Acceptance ratio
α_{PT}	Acceptance ratio of parallel tempering
α_{RJ}	Acceptance ratio of RJMCMC
α_{SA}	Acceptance ratio of SA coupled RJMCMC
β	Scaling parameter
ϵ	Error term

$\hat{R}$	Potential scale reduction factor
λ	Regularization parameter
Σ	Noise covariance
σ_B^2	Between chain variance
σ_W^2	Within chain variance
σ_E	Noise standard deviation
θ	Dipole location and magnitude parameter set

LIST OF ABBREVIATIONS

ANOVA	Analysis of Variance
ABIC	Akaike Bayesian Information Criterion
AP	Action Potential
BEM	Boundary Element Method
BOLD	Blood Oxygen Level Dependent
BA	Brodmann Area
COG	Center of Gravity
CSD	Current Source Density
ECD	Equivalent Current Dipole
EEG	Electroencephalography
EDL	Estimated Dipole Location
EDN	Estimated Dipole Number
EP	Evoked Potential
EPI	Echo Planner Imaging
ERP	Event-Related Potential
F	Face Stimulus
fMRI	Functional Magnetic Resonance Imaging
FG	Fusiform Gyrus
FWE	Family Wise error
HRF	Hemodynamic Response Function
HEOG	Horizontal Electrooculogram
IN	Iteration Number
LE	Localization Error
LO	Local Optima
LORETA	Low Resolution Electromagnetic Tomography
MAP	Maximum A Posteriori
MCMC	Markov Chain Monte Carlo
MEG	Magnetoencephalography

MIP	Maximum Intensity Projection
MNI	Montreal Neurology Institute
MRI	Magnetic Resonance Imaging
MUSIC	Multiple Signal Classification
PET	Positron Emission Tomography
PSP	Post Synaptic Potential
PSRF	Potential Scale Reduction Factor
PT	Parallel Tempering
PT-RJMCMC	Parallel Tempering coupled Reversible Jump MCMC
SNR	Signal to Noise Ratio
ReML	Restricted Maximum Likelihood
RJMCMC	Reversible Jump Markov Chain Monte Carlo
S	Scrambled Face Stimulus
SA	Simulated Annealing
SA-RJMCMC	Simulated Annealing coupled Reversible Jump MCMC
SPECT	Single Photon Positron Emission Tomography
SPM	Statistical Parametric Mapping
SVD	Singular Value Decomposition
TIK	Tikhonov Regularization
VEOG	Vertical Electrooculogram

1. INTRODUCTION

1.1 Motivation

The electroencephalogram, EEG is a record of the oscillations of brain electrical potential recorded from electrodes on the scalp. The scalp EEG, consisting of measurements of a set of electric potentials differences between pairs of scalp provides very large scale and strong measures of neocortical activities. Although electrical activity recorded from the exposed cerebral cortex of a monkey was reported in 1875 by Caton, it was not until 1929 that Hans Berger, a psychiatrist in Jena, Germany first recorded rhythmic electrical activity from the human head. Since then, EEG has become one of the most prominent methods for noninvasive examination of brain activity [1]. Besides spontaneous EEG recording, some associated measurements have also been widely practiced. For example the event-related potentials (ERPs) measure the brain responses that are time-locked to an external stimulus or an internal cognitive event, whereas its subclass, the evoked potentials (EPs), are usually elicited in response to sensory stimuli.

Brain electrical activation is a spatiotemporal process, which means that the activity is three-dimensionally distributed in the brain tissue and evolves with time. Localizing the different modules of the functional network implicated in a given mental task is the main purpose of functional neuroimaging studies. During the last 20 years, research using functional imaging techniques, first with single photon positron emission tomography (SPECT) and positron emission tomography (PET), and then with functional magnetic resonance imaging (fMRI) are widely done. Neural activation can be detected *indirectly* with both fMRI and PET through imaging of localized contrast changes that result from the hemodynamic effects of this activation. PET and fMRI provide millimeter scaled spatial resolution but their temporal resolutions are severely limited by relatively slow responses of brain metabolism [2]. To investigate temporal properties of brain circuits, methods that directly measure neuronal activity in real

time are needed. EEG with its millisecond-scale temporal resolution offers this possibility. Its temporal resolution is only limited by the time scale of the biological process. On the other hand, the conventional EEG suffers from its limited spatial resolution. This limitation is mainly due to two factors:

(i) One factor is the limited spatial sampling. The standard 10/20 EEG recording montage results in the interelectrode distance of about 6cm. A remarkable progress in the past decade is that high-resolution EEG systems with 64 to 256 electrodes have been commercially available. For example, with up to 124 electrodes the average interelectrode distance can be reduced to about 2.5 cm. However, EEG data become highly correlated when the interelectrode distance is reduced about 1 cm. It is reported that the resolution increases linearly with increasing number of electrodes, reaching a plateau at around 100 electrodes [3] .

(ii) The second factor is the head volume conduction effect. A single electrode provides estimates of synaptic action averaged over tissue masses containing between approximately 100 million and 1 billion neurons. The space averaging of brain potentials resulting from extracranial recording is a random data reduction process forced by current spreading in the head volume conductor. The electrical potentials generated from neural sources are attenuated, distorted and blurred as they pass through the neural tissue, cerebrospinal fluid, meninges, and the low-conductivity skull, and scalp. Especially the contribution of the low-conducting skull is significant. This physical separation of the electrode and brain current sources limits the spatial resolution of EEG.

Advanced EEG imaging techniques are required to compensate for the head volume conduction effect and enhance the spatial resolution of the EEG. The most commonly applied spatial enhancement technique is the *EEG source reconstruction*. Given a set of scalp measurements, EEG source reconstruction process involves estimation of the properties of the current sources within the brain that produced that signals. This localization process needs the solutions of two separate but closely related problems, EEG forward problem and EEG inverse problem (Figure 1.1) which is the

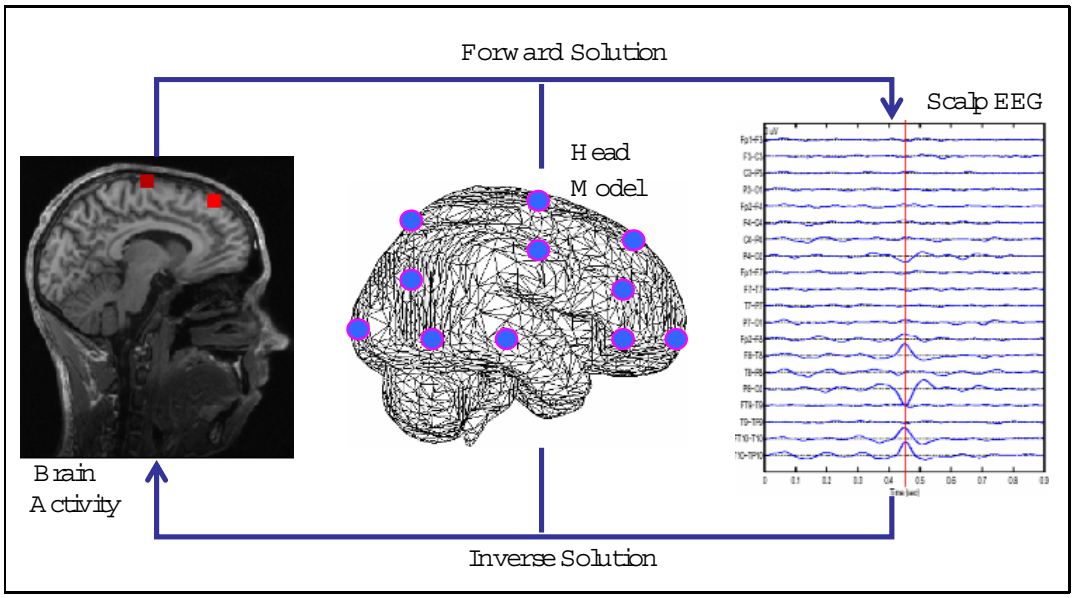

Figure 1.1 EEG source localization is done by solving forward and inverse problems. Given a head model and neural source configuration, forward solution determines produced scalp potentials. Given scalp potentials and a head model, inverse solution determines neural sources.

main topic of this thesis.

The ultimate goal of electrophysiological neuroimaging is to image brain electrical activity with a high resolution in both time and space domains based on noninvasive EEG recordings. Such noninvasive and high resolution brain imaging techniques would bring significant advancement in the fields of clinical neurosurgery, neural pathophysiology, cognitive neuroscience, and neurophysiology. For example, in planning tumor and epilepsy surgery, precise localization of the areas causing symptoms has substantial importance.

EEG source imaging can facilitate presurgical planning, delineate the epileptic zone in seizure patients, characterize the brain dsyfunction in patients with psychiatric disorders and Alzheimer, localize and image brain regions contributing to cognitive tasks, and help understand how the “Mind” works.

1.2 Objectives

By assuming that neural sources are dipoles aligned in large groups which generate an electric current corresponding temporally and spatially to brain activity, EEG dipole source localization can be realized by solving the forward and the inverse problem using numerical methods.

Given the information on the brain electric source distribution and the head volume conduction properties, the EEG forward problem determines the source-generated electric field. The EEG forward solution can be electric potentials, such as the cortical potentials or scalp potentials, or other measures, like the current density distribution Figure 1.1. The EEG forward problem is well-defined and has a unique solution governed by the quasi-static limit of Maxwell's equations [4]. Different scalp topographies must have been generated by different source configurations. By solving the forward problem, the EEG measurements and the underlying brain electrical sources can be related by the lead field matrix, which is only dependent on the head model and electrode placements.

In terms of geometry, the head model conductor can be represented by simple spherical models, or by realistically shaped head models. Spherical models involve an analytical formulation for the computation of the forward problem. Realistic models are usually implemented by the numerical methods such as the boundary element method (BEM), the finite element method, the finite volume method, the finite difference method, and so on [5]. The accuracy of the head model and its forward solution has substantial effects on the accuracy of the source localization process. Spherical models are generally insufficient for the localization of an arbitrary dipole in the brain. For superficial dipoles locating in brain regions where the spherical model fits well locally, source localization results in few millimeter errors. Whereas, for deep sources and other brain regions the localization errors are up to several centimeters. Localization error decreases with the use of realistic models where anatomical information is obtained from high resolution magnetic resonance imaging (MRI) [2].

In this thesis, realistic head model and forward solution that had been developed in previous studies [6, 7] and provided accurate solutions [6, 7, 8, 9] is used.

Given the known electrical field and head volume conductor properties, the EEG inverse problem estimates the location and strength of the brain electrical sources (Figure 1.1). Unlike the forward problem, the EEG inverse problem is ill-posed in that there are an infinite number of source configurations that could explain a given data set of scalp potential measurement. The ill-posedness, high computational cost, and other complications of the electromagnetic inverse problem pose significant technical challenges.

Many methods have been developed for the solution of the EEG inverse problem with the majority of which restate it as a least-squares minimization problem. The inverse problem is formulated with either a parametric approach, where sources are presented by a few equivalent current dipoles or with a imaging approach which assumes distributed currents in the brain. Methods based on Bayesian approach are first introduced in 1997 by Sylvian Baillet [10] and James W. Philips [11] and applied on magnetoencephalogram (MEG) with spherical head models. During the past 10 years, Bayesian formulation of the electromagnetic inverse problem has drawn substantial interest in the neuroimaging research community. The fast development of computing power has enabled the use of Markov Chain Monte Carlo (MCMC) methods and further boosted probabilistic formulations to electromagnetic inverse problem [12], [13]. However, no gold standard exists for the reconstruction of the scalp EEG generators.

Our objective in this study is to combine the Bayesian methodology and MCMC methods to provide source reconstruction that will address the ill-posed character of the EEG inverse problem. For this purpose an effective MCMC algorithm with parameters tuned to this specific problem is designed. To produce a sampling of many likely solutions from posterior dipole parameter distributions without getting trapped in to local optima, heuristic methods are coupled to the MCMC sampler. The feasibility of the MCMC method is investigated with simulated data obtained by different dipole configurations. Application to realistic data is also performed. Regarding to lo-

calization errors and comparisons with other widely used inverse solutions, this study shows that Bayesian MCMC methods are well suited to the solution of the EEG inverse problem and gives highly promising results for the accurate reconstruction of the EEG sources.

1.3 Outline of the Thesis

The outline of the thesis is as follows: In Chapter 2, the physiological basis and methods in the EEG inverse problem are presented. Chapter 3 includes the Bayesian formulation of the problem. In Chapter 4 details of MCMC and heuristic methods used to sample the posterior distributions are presented. The proposed inverse method has been evaluated with simulated EEG and empirical ERP data in Chapter 5 and Chapter 6, respectively. Finally, the discussions and the conclusions are presented in Chapter 7.

2. THE INVERSE PROBLEM IN EEG SOURCE ANALYSIS

2.1 Generators of the EEG

The electrodes used in scalp EEG are large and remote so that they only measure extracellular current flow due to the summated activity of a large number of neurons which are *synchronously* active. To understand the nature of voltages that can be recorded at the scalp, it is necessary to understand the current distributions generated inside the brain.

There are two main types of electrical activity associated with neurons, action potentials (AP) and postsynaptic potentials (PSP). APs are discrete voltage spikes that travel from the beginning of a axon at the cell body to the axon terminals. APs can be large in amplitude (70-110 mV) but they have a small interval of time (0.3 ms). A synchronous firing of APs of neighboring neurons is unlikely. When an AP reaches a synapse and generates a PSP, the ion flow causes an electrical field and current along the interior of the postsynaptic neuron. PSP amplitudes are smaller (0.1-10 mV) but their relatively large interval of time (10-20 ms) enables the neighboring neurons to generate a summated activity. The ionic current flowing within the elongated process of the neuron is called the *primary current*. The charge conservation law states that the primary current is compensated by passive ohmic currents, called the *volume currents* or *secondary currents*, in the surrounding tissue as shown in Figure 2.1 [14]. EEG would not be possible without volume currents, which can reach the scalp surface and cause voltage differences that can be picked up by EEG electrodes.

So, the current density $\vec{J}$ at location $\vec{r}$ inside the head volume, can be split into primary currents $\vec{J}^p$ and volume currents $\vec{J}^v$ which are generated by the effect of electrical field on extracellular charges at location $\vec{r}$:

$$J(\vec{r}) = J^p(\vec{r}) + J^v(\vec{r}) = J^p(\vec{r}) + \sigma(\vec{r})E(\vec{r}) \tag{2.1}$$

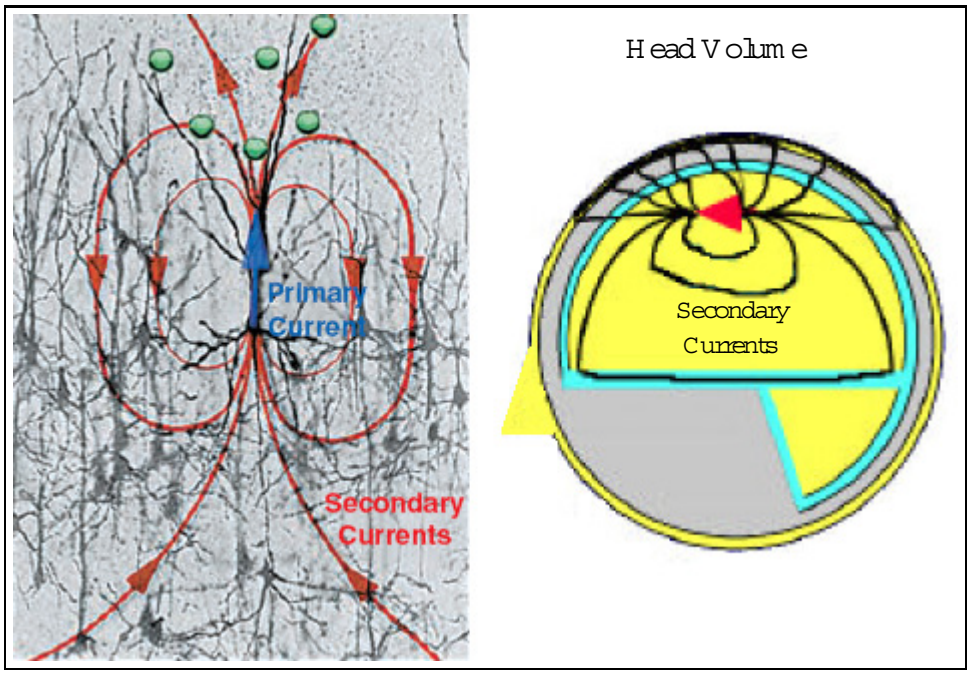

Figure 2.1 Primary and secondary currents generated by PSPs.

.

where σ is the conductivity and E is the electrical field. In EEG inverse problem we try to locate primary currents that can be approximated with a current *dipole*.

Besides having more or less synchronous activity, the neurons need to be regularly arranged to have a measurable scalp EEG signal. The spatial properties of the neurons must be so that they amplify each other's extracellular potential fields. If the dendrites supporting PSPs are randomly oriented on a small cortical surface, no net electromagnetic field can be detected. For example, cortical stellate cells occupy roughly spherical volumes such that the associated synaptic sources provide a "closed field" structure: They are electrically invisible to scalp electrodes [15].

In the cortical gray matter the cells are arranged in six layers, as illustrated in Figure 2.2 [16]. The thickness of the cortical gray matter varies between 1 mm and 4 mm. Two large pyramidal cells consisting of apical and basal dendrites are visualized in Figure 2.2. The apical dendrites are located in the outermost layers 1 and 2 of the cortical gray matter. The basal dendrites are located in layers 3-5 of the cortical gray matter. Pyramidal cells contain dendiritic spines and are the only output neurons in

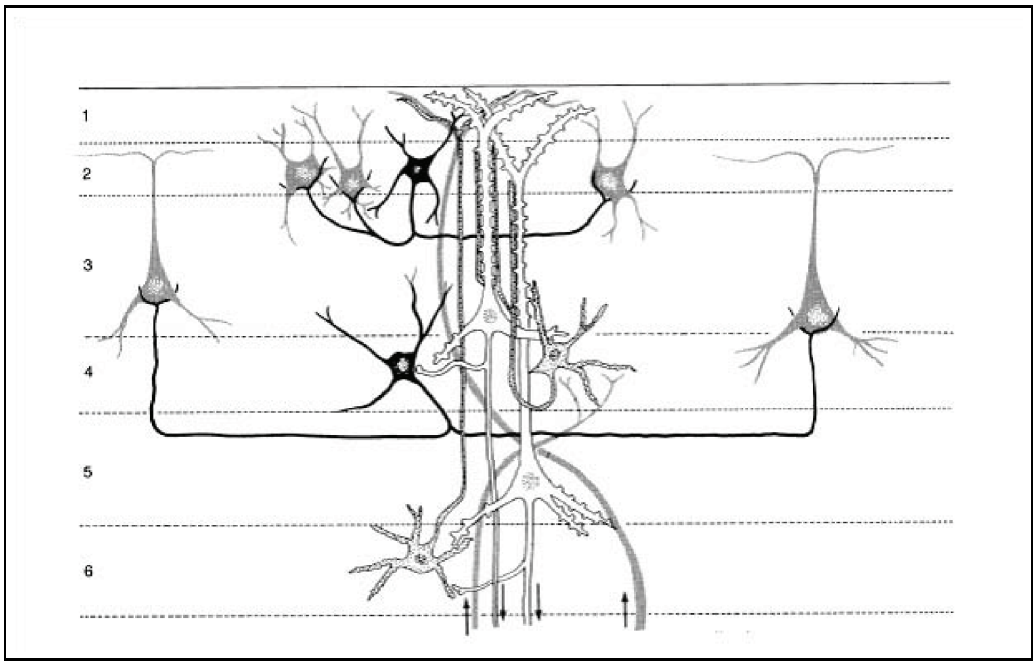

Figure 2.2 The layered cortex. The white cells correspond with pyramidal cells.

the cortex [16].

The neighboring pyramidal cells are organized so that the axes of their dendrite tree are parallel with each other and orthogonal to the cortical surface. Hence, these cells are suggested to be the generators of the EEG [1, 2, 17, 16]. Having revealed substantial vertical, but little local horizontal variation in potential, subdural and intracortical recordings of field potentials at varying distances from an activated cortical locus are consistent with this suggestion [18, 19, 20]. Calculations shown in [21] suggest that each synapse along a dendrite may contribute as a 20 fA-m current source and cortex macrocellular current density is in the order of 100nA/mm^2. If we assume the cortex is about 4 mm thick, then a small patch $5mm \times 5mm$ would yield a net current of 10 nAm, consistent with empirical observations and invasive studies [2].

Although the scalp EEG predominantly reflects the activity of cortical neurons close to the electrode sites, scalp observations of electrical activity from deeper cortical areas, such as the hippocampus [22, 23], cerebellum [24], thalamus [25], brainstem [26] and amygdala [27] are reported. Contributions from deep structures to scalp EEG, not necessarily direct, may be taken into account during source localization processes.

2.2 General Concerns in EEG inverse problem

The inverse problem of reconstructing the neural electrical current that produced a given measurement is ill-posed and many different source configurations can yield the same EEG potentials. Moreover, the inverse solution suffers from instability, which means that small variations in the measurements can lead to large changes in the solution. The fundamental problem of EEG source reconstruction is this *ambiguity* of the electromagnetic inverse problem.

To obtain a unique inverse solution additional constraints have to be imposed, such as anatomical, physiological, spatiotemporal, and/or functional constraints provided by other imaging modalities. These "a priori" assumptions are crucial as they directly determine the solution space. Based on some constraints, an inverse solution can explain a given data set but it may not necessarily give neurophysiological information about where the signals were generated exactly. Moreover, even if it is mathematically possible to reformulate the EEG inverse problem in a well-posed form, some "malign" type of ill-posedness, like the situation when two neighboring sources cancel each other, will remain. Since all information about neuronal signal generation has yet to be revealed, there has been intensive research to develop a universally accurate method for the source localization problem.

Recent studies use specific anatomical and physiological constraints in a Bayesian framework that is especially well-suited to the probabilistic nature of the available "a priori" information. Some of them keep trying to find a single best solution [28, 29, 10, 11] that does not take into account the ambiguity of the problem. On the other hand, with the introduction of MCMC methods in source imaging research, probabilistic solutions permit monitoring many likely sources to address the ill-posedness [12].

To illustrate the lack of uniqueness of the EEG inverse problem, we produced an instantaneous EEG data with 10 dB signal to noise ratio (SNR) and solved the inverse problem with different methods and with different assumptions for the same

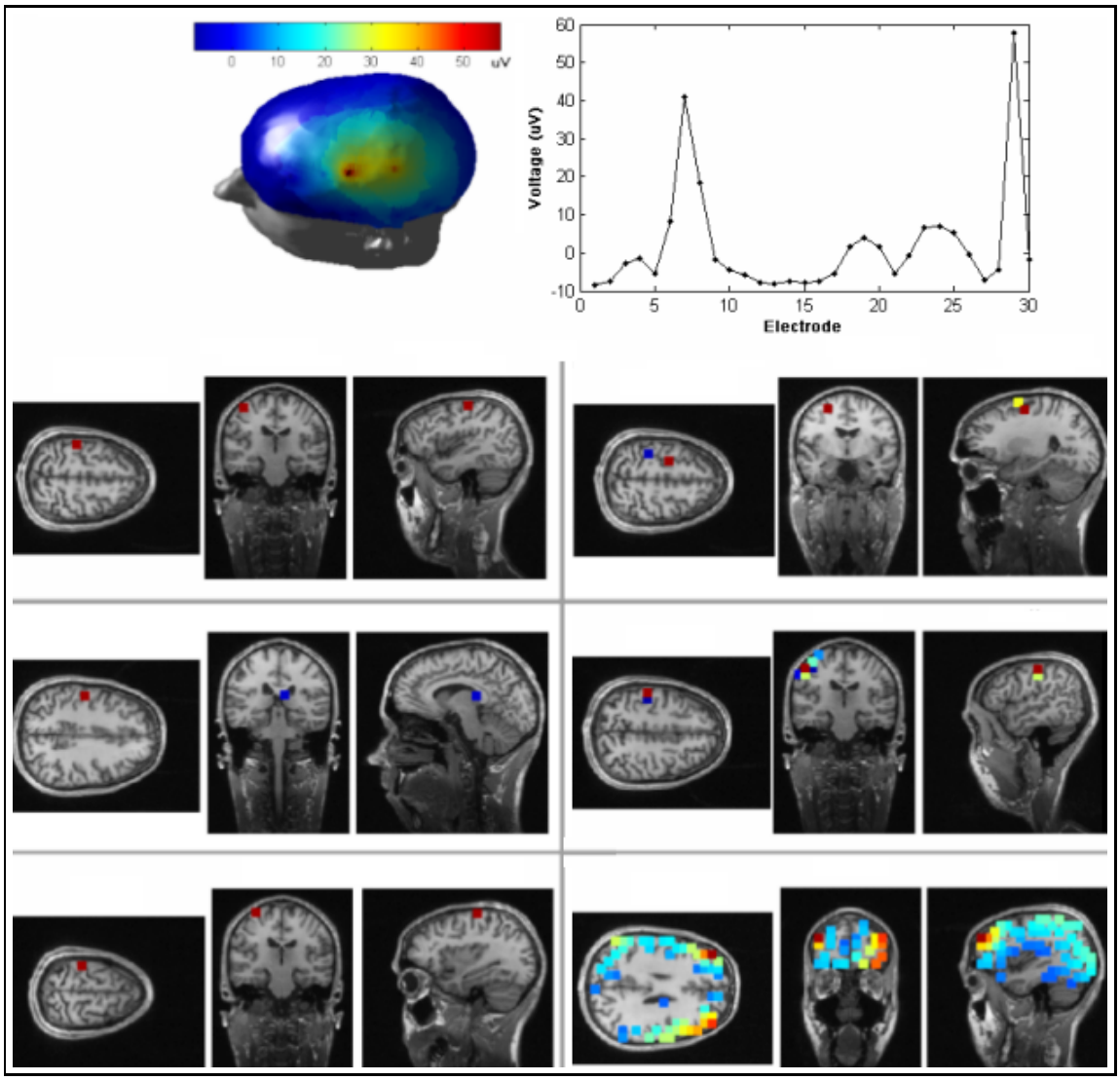

Figure 2.3 Lack of uniqueness in the inverse problem: Each panel shows three views of source configurations that can produce the same EEG data and scalp topography shown at the top. Markers with different colors correspond to different dipole sources.

method. Figure 2.3 shows six source configurations, with different moment and location parameters, that can produce the same EEG voltage distribution and scalp topography.

2.3 Methods in the EEG inverse problem

In terms of dimensionality of the solution space, the EEG inverse solution can be classified to equivalent current dipole (ECD) model (also called *parametric model-*

ing) and the distributed source model [2]. Another classification can be made upon the dimension of the EEG data set. One approach is the single time-slice, instantaneous source localization, in which the dipole parameters are fitted at an instance in time, based on the single time "snapshots" of the measured scalp EEG. Another approach is the multiple-time slice source localization, also termed spatiotemporal source localization, by incorporating both the spatial and temporal components of the EEG in model fitting.

In this study, our analysis covers both ECD and distributed approaches but limited to instantaneous source localization.

2.3.1 ECD modeling of inverse problem: MUSIC

ECD model assumes that the scalp EEG is generated by one or a few focal sources. Each of the focal sources can be modeled by an equivalent current dipole with six parameters: three location parameters and three directional parameters. When this six parameters are free to change independently, it is called a *moving dipole*.

In the ECD approach the scalp potentials at the single time-slice are collected into a column vector $\vec{F}$, each row of which is the potential data recorded from one electrode. The problem is then to find a column vector $\vec{V}$, the collection of the potentials at the same electrode but generated by assumed dipole sources inside the brain. In practice, an initial starting point (seed) is estimated, then using an iterative procedure, the assumed dipole sources are moved around inside the brain in attempt to produce the best match between $\vec{V}$ and $\vec{F}$. This involves solving the forward problem repetitively and calculating the difference between measured and estimated potentials vectors in each step. The most commonly used measure is the squared distance between the two vectors, which is given by

$$\vec{E} = \|\vec{F} - \vec{V}\|^2 \tag{2.2}$$

where $\vec{E}$ is the objective function to be minimized. Dipole sources are coupled to the

scalp potentials $\vec{V}$ by the lead field matrix K using the forward formulation. If we have N_e different measurement sites in the conductor model, the forward problem can be formulated by the electrical potential $V\ (\vec{s})$ at electrode location $\vec{s}$ due to a dipole at $\vec{r}$ with strength $\vec{m}$ as in Eq. 2.3

$$V(\vec{s}) = \sum_{i=1}^{N} K(\vec{s}, \vec{r_i}) m(\vec{r_i}) + \vec{\varepsilon}. \tag{2.3}$$

Here, $V\ (\vec{s})$ is $N_e \times 1$ electrical field vector, N is the number of dipoles which are synchronously active, $\vec{m}$ is a 3×1 strength vector for a single current dipole source located at $\vec{r}$ and $K(\vec{s}, \vec{r})$ is a $N_e \times 3$ dimensional transfer function which depends on the dipole location $\vec{r}$, the measurement sites $\vec{s}$, and the geometrical and physical properties of the media. $\vec{\varepsilon}$ is $N_e \times 1$ additive measurement noise.

Multiple Signal Classification algorithm (MUSIC) on EEG inverse problem is an example for ECD approach. In the following chapters we use MUSIC to compare its results with those of Bayesian MCMC source localization.

MUSIC algorithm scans the 3D brain tissue for the moving dipoles by spatial spectral estimation.

In MUSIC, the eigendecomposition of the EEG data is used to estimate the number of active dipoles that produce measured potentials. Assuming that there are P independent dipole sources, the eigendecomposition of $\vec{V}$, which is a N_e by T time-slices EEG data matrix will generate P eigenvalues arising from the signal sources and $N_e - P$ eigenvalues arising from the noise, and their corresponding eigenvectors span the signal subspace and noise subspace, respectively. Because the lead field vector at each source location should be orthogonal to the noise subspace, the locations of dipoles can be estimated by evaluating a spectral measure at each possible spatial location. This scan metric measures the orthogonality between the lead field vector and the noise subspace, and the locations that produce a peak in the scan metric are chosen as probable source locations. A recursive approximation method (RAP-MUSIC) has also been proposed in order to overcome the "multiple-peak picking" problem of the

original MUSIC scan [30].

If $\vec{V}$ is an instantaneous EEG data, the rank is always equal to one and MUSIC finds a single dipole whose location and moment parameters match the measured potentials. This ad-hoc assumption on the number of sources may cause MUSIC to fail when multiple sources are synchronously active.

MUSIC has been demonstrated to be useful in locating the focal sources such as those in some epilepsy cases, especially when it is combined with time-frequency methods for preprocessing [31]. On the other hand, its major limitation is that its simplified source model can not adequately describe sources of significant spatial extent.

2.3.2 Distributed modeling of inverse problem: LORETA

As ECD approaches have difficulties describing widespread neural activity as in the case of cognitive processes and certain pathologies, distributed source imaging, also called imaging approach has been studied in the past decade, particularly when studying higher-order brain functions.

Imaging approaches consist of estimating the magnitude of a predefined dense set of dipoles, typically distributed all over the 2D cortical sheet or 3D volume of the brain. Source locations are fixed, N is much larger than N_e, so that Eq. 2.3 becomes underdetermined but linear :

$$\vec{V} = K\vec{J} + \vec{\varepsilon} \tag{2.4}$$

where $\vec{J}$ is a vector representing the current dipoles at all the N locations, and K is the lead field matrix and $\vec{\varepsilon}$ is the additive measurement noise. The source orientation is left free so that $\vec{J} = \left[\vec{j}_1, \vec{j}_2 \ldots \vec{j}_{n_d}\right]^T$, where $\vec{j}_i = [j_{x_i}, j_{x_i}, j_{z_i}]^T$ encodes both orientation and amplitude of the i^th current dipole. The aim of the imaging approach is to design

an inverse filter B which can project the measured data into the solution space:

$$\vec{J} = B\vec{V} \tag{2.5}$$

When the rank of K is less than the number of its rows, KK^T is singular and its inverse does not exist. In such a case, the general inverse can be sought by the method of singular value decomposition (SVD). For an $N_e \times N$ matrix K, the pseudo-inverse $K^\dagger$ of is given by

$$K^\dagger = \vec{V}\Sigma^{-1}\vec{U}^T = \sum_{i=1}^{p} \frac{1}{\lambda_i} v_i {u_i}^T \tag{2.6}$$

where $\vec{U} = [u_1, u_2, \ldots, u_{N_e}]$, $\vec{V} = [v_1, v_2, \ldots, v_N]$,$\Sigma = diag(\lambda_1, \lambda_2, \ldots, \lambda_p)$, $\lambda_1 > \lambda_2 > \ldots > \lambda_p$ and $p = min(N_e, N)$. The vectors u_i and v_i are orthonormal eigenvectors of KK^T and K^TK respectively and the λ_i are the singular values of K. $(\cdot)^T$ denotes the inverse of a matrix.

This general inverse solution is often impractical for real applications because of the ill-posed nature of the EEG inverse problem. Small measurement errors will be amplified by the small or near-zero singular values, leading to large perturbations in the inverse solution as given in Eq. 2.6.

A common approach to overcome this numerical instability is the Tikhonov regularization (TIK), in which the inverse filter is designed to minimize an alternative objective function that is uniquely solvable and robust in the sense that small errors in the data do not corrupt excessively this approximate solution:

$$\vec{J}_{TIK} = \|\vec{V} - K\vec{J}\|^2 + \lambda^2 \|G\vec{J}\|^2 \tag{2.7}$$

where λ is the regularization parameter, G can be the identity, gradient, or Laplacian matrix, corresponding to 0^{th}, 1^{st} and 2^{nd} order TIK respectively. When $\lambda = 0$ Eq. 2.7 corresponds to *minimum norm least-squares* inverse solution.

Low Resolution Electromagnetic Tomography (LORETA) [32] corresponds to

the 2^{nd} order TIK where $G = L$, the Laplacian operator which has the form of Eq. 2.8

$$L = (I_N - \frac{1}{6}N_v) \otimes I_3 \tag{2.8}$$

where I_N is the identity matrix with the dimension of number of voxels (N) in the solution space and N_v is the number of neighbor voxels of each voxel in the solution space. For some voxels, it is not possible to find all the six predefined neighbors, so the number of orthogonal neighbors N for each voxel in the solution space has to be computed. LORETA inverse filter has the form:

$$B_{LORETA} = (K^T K + \lambda^2 L^T L)^{-1} K^T \tag{2.9}$$

where λ variable should be written as a product term rather than addition in order to optimize the process. Therefore, singular value decomposition of KL^{-1} is defined as $KL^{-1} = USV^T$. Using the $K = USV^T L$ relation, Eq. 2.9 can be written as:

$$B_{LORETA} = (L^T VSU^T USV^T L + \lambda^2 L^T L)^{-1} L^T VSU^T \tag{2.10}$$

Eq. 2.10 is identical with Eq. 2.11.

$$B_{LORETA} = [L^T V(S^2 + \lambda^2 I)V^T L]^{-1} L^T VSU^T \tag{2.11}$$

By using De Morgan's law, Eq. 2.11 can be rewritten as in Eq. 2.12.

$$B_{LORETA} = L^{-1} V(S^2 + \lambda^2 I)^{-1} V^T (L^T)^{-1} L^T VSU^T \tag{2.12}$$

Finally, Eq. 2.12 can be shown as in Eq. 2.13.

$$B_{LORETA} = L^{-1} V diag(\frac{S_{ii}}{S_{ii} + \lambda^2}) U^T \tag{2.13}$$

where $diag(\cdot)$ is a diagonalizing operator.

The regularization parameter λ is obtained using Akaike Bayesian Information Criterion (ABIC) [33]:

$$ABIC(\sigma_\epsilon, \sigma_\epsilon/\lambda) = (-2) log L_{II}(\sigma_\epsilon, \sigma_\epsilon/\lambda) \tag{2.14}$$

By maximizing Eq. 2.14, σ_ϵ and λ can be found for a given EEG data.

$$logL_{II}(\sigma_\epsilon, \lambda) = \sum_{i=1}^{N_e} log(\frac{S_{ii}^2 + \lambda^2}{\lambda^2}) N_e(1 + log 2\pi\sigma_\epsilon^2) \tag{2.15}$$

where the estimate of the observation noise variance σ_ϵ^2 is given by Eq. 2.16

$$\sigma_\epsilon^2 = \frac{1}{N_e} \sum_{i=1}^{Nc} \frac{\lambda^2}{S_{ii}^2 + \lambda^2} Y_i^{-2} \tag{2.16}$$

where $Y_i = U^T \vec{V}_{EEG}$.

LORETA method selects the solution with a smooth spatial distribution by minimizing the Laplacian of weighted sources. The physiological reasoning underlying this constraint is that activity in neighboring neurons is correlated. However, it is known that functionally very distinct areas can be anatomically very close. As conventional LORETA implementations do not take such anatomical distinctions into account, smoothness constraint of the LORETA approach can cause "ghost sources" to appear in the solution. Ghost sources are defined as additional sources in the solution that do not make much physiological sense and obscure the interpretation of the results.

3. BAYESIAN MODELING OF THE EEG INVERSE PROBLEM

At the core of Bayesian way of thinking is the Bayes theorem, which maintains, in its simple interpretation, that's one belief about the world should be updated according to the product of what one believed in before and what evidence has come to light since.

Bayesian approach differs from classical methods by that the unknown parameters of interest are no longer assumed to be *deterministic* but *random*. Deterministic inverse techniques lead to point estimates of unknowns without rigorously considering the statistical nature of system uncertainties and without incorporating prior knowledge. Bayesian approach provides not only point estimates but also the probability distribution of the unknown quantities conditional on available data.

3.1 Fundamentals of Bayesian Inference

Bayesian inference is the process of fitting a probability model to a set of data and expressing the result by a probability distribution on the parameters of the model and on unobserved quantities such as predictions for new observations [34]. The key idea underlying Bayesian philosophy is that all forms of uncertainty are expressed in terms of probability. A Bayesian approach to a problem can be summarized by three steps.

(i) First step is to set up a probability model namely a joint probability distribution for all observable and unobservable quantities in a problem. Given observed data y and unknown parameter θ the joint probability mass or density function $p(\theta, y)$ can be written as a product of two densities that are often referred to as *the prior*

distribution $p(\theta)$ and *the likelihood function* $p(y|\theta)$ respectively:

$$p(\theta, y) = p(\theta)p(y|\theta) \tag{3.1}$$

Conditioning on the known value of the data y, using the basic property of conditional probability known as *Bayes' rule*, we have the posterior density:

$$p(\theta|y) = \frac{p(\theta, y)}{p(y)} = \frac{p(\theta)p(y|\theta)}{p(y)} \tag{3.2}$$

Since $p(y)$ is independent of θ, it can be considered a normalizing constant and can be omitted from the *unnormalized posterior density*:

$$p(\theta|y) \propto p(\theta)p(y|\theta) \tag{3.3}$$

where $p(\theta)$ is prior probability, which is get before receiving any data. $p(\theta|y)$ is called *posterior probability*, which is obtained after those data coming. Hence, to set up a probability model for the EEG inverse problem based on Bayesian inference, we should first find the likelihood function that describes the interrelation between the scalp potentials and the unknown brain activity, and which is based on all the prior information of the unknown, find a prior probability density.

(ii) The second step in the Bayesian approach is to develop methods to explore the posterior probability density. The Chapter 4 deals completely with this step where MCMC methods are used.

(iii) Evaluating the fit of the model and implications of the resulting posterior distribution is the final step of Bayesian approach. In the EEG inverse problem, this is equivalent to investigating the feasibility of the resulting source reconstruction method with simulated and realistic EEG data.

3.2 Bayesian Inference Applied to the EEG Inverse Problem

The spatial EEG dipole analysis based on Bayesian inference is formulated in the following way: assuming a localized effective dipole nature of neural sources that could explain the instantaneous EEG data, we construct a current model that assumes a variable number of current dipoles composed of different locations within a realistic head model and dipole moments. Unknown neural activity parameters are:

- N: *a priori* unknown number of active dipoles,
- $\vec{r}$: location(s) of dipole source(s),
- $\vec{m}$: magnitude(s) of dipole moments.

The analysis is limited to a *single instant of time* so that dipole parameters are not time-dependent.

Given EEG measurements at a single point in time acquired on N_e electrodes, the Bayesian formulation is as follows:

$$p(N, \vec{r}, \vec{m}|\vec{V}) \propto p(\vec{V}|N, \vec{r}, \vec{m})p(\vec{r}|N)p(\vec{m}|N)p(N). \tag{3.4}$$

where $\vec{V}$ is the set of measurements at N_e electrodes, N is the *priori* unknown number of dipole sources which are active in the same instant, $\vec{r} = (r_1, \ldots, r_N)$ is the location vector of N dipole sources, with each $\vec{r_i}$ being equal to a triplet $\{r_{x_i}, r_{y_i}, r_{z_i}\}$ representing the position of the ith active dipole in the head model. $\vec{m} = (m_1, \ldots, m_N)$ is the dipole moment magnitude, with each $\vec{m_i}$ being equal to a triplet $\{m_{x_i}, m_{y_i}, m_{z_i}\}$ representing moment parameter which also codes dipole orientation. Here, generators of the EEG are not restricted to the cortex, namely to pyramidal cells as mentioned in Chapter 2. It is assumed that non-cortical areas can contribute to scalp potentials; radial orientation is no longer a restriction so that dipole orientation is left free.

3.2.1 Construction of the Likelihood Function

The likelihood function $p(\vec{V}|N,\vec{r},\vec{m})$ contains *the forward EEG model* and information about the noise. The additive measurement noise $\vec{\varepsilon}$ defined in Eq. 2.3 is assumed to be N_e-variate Gaussian with zero mean and covariance matrix Σ. The mutual independence of $\vec{\varepsilon}$ and dipole parameters assures that the probability density of $\vec{\varepsilon}$ remains unaltered when conditioned on unknowns. Hence, the likelihood function is expressed as:

$$p(\vec{V}|N,\vec{r},\vec{m}) = \frac{1}{(2\pi)^{\frac{N_e}{2}}|\Sigma|^{\frac{1}{2}}}\exp(-\frac{1}{2}[\vec{V}-\sum_{i=1}^{N}K(\vec{r_i})\vec{m_i}]^T\Sigma^{-1}[\vec{V}-\sum_{i=1}^{N}K(\vec{r_i})\vec{m_i}]) \quad (3.5)$$

where $K(\vec{r_i})$ is the transfer function by $N_e \times 3$ for the i^{th} active dipole locating at $\{r_{x_i}, r_{y_i}, r_{z_i}\}$ and $\vec{m_i}$ is 3×1 moment vector.

3.2.2 Prior Models

The second term $p(\vec{r}|N)$ at the left-hand side of Eq. 3.4 represents *a priori* knowledge about the location of dipole sources without considering any given EEG measurements. In this study, dipole locations are constrained on anatomical surfaces, deduced from average T1 weighted human brain MRI data provided by Montreal Neurology Institute (MNI). The main motivation is to prevent solutions from being found in unrealistic locations (i.e., in the white matter for instance).

Dipole locations are restricted to the gray matter. A voxel of the MR image is labeled as a gray matter if it satisfies three conditions: Its probability of being gray matter is higher than that of being white matter, its probability of being gray matter is higher than that of being white matter and cerebrospinal fluid. And the final constraint is taken as probability of being gray matter is higher than 0.66.

Having N_v voxels locating in the gray matter volume of the brain, the dipole location prior distribution is chosen to be uniform over N_v:

$$p(\vec{r}|N) = \begin{cases} (\frac{1}{N_v})^N & \{r_{x_i}, r_{y_i}, r_{z_i}\} \in Head(N_v) \forall i, \\ 0 & \text{otherwise.} \end{cases} \tag{3.6}$$

where $Head(N_v)$ is a realistic head model with N_v voxels.

$p(\vec{m}|N)$ represents a prior probability distribution of dipole moments strength. Prior for dipole moments are chosen to be uniform between m_{min} and m_{max}.

The last term, $p(N)$ corresponds to the model probability for the number of active dipoles. We assumed a uniform law, for N between predefined minimum and maximum number of dipoles,

$$p(N) = \frac{1}{N_{max} - N_{min} + 1} \tag{3.7}$$

Finally, the Bayesian formulation for the instantaneous EEG source reconstruction problem is:

$$\begin{aligned} p(N, \vec{r}, \vec{m}|\vec{V}) \propto & \left[(2\pi)^{\frac{N_e}{2}} |\Sigma|^{\frac{1}{2}} (N_{max} - N_{min} + 1) \left(N_v (m_{min} - m_{max} - 1)\right)^N\right]^{-1} \\ & \times \exp\left(-\frac{1}{2}\left[\vec{V} - \sum_{i=1}^{N} K(\vec{r_i})\vec{m_i}\right]^T \Sigma^{-1} \left[\vec{V} - \sum_{i=1}^{N} K(\vec{r_i})\vec{m_i}\right]\right) \end{aligned} \tag{3.8}$$

4. SOLUTION OF THE BAYESIAN MODEL BY MARKOV CHAIN MONTE CARLO (MCMC) METHODS

Having expressed the EEG inverse problem in a probabilistic way, we explored MCMC methods to sample the posterior probability $p(x|\vec{V})$ with x being the set of parameters:

- N: *a priori* unknown number of active dipoles
- $\vec{r}$: location(s) of dipole source(s)
- $\vec{m}$: magnitude(s) of dipole moments

4.1 Why Using MCMC Methods in EEG Inverse Problem?

The interpretation of the posterior distribution as the solution of an inverse problem is a subtle issue. The statistical solution of an inverse problem can be used to produce *single estimates* as in the classical inversion methods. In the probabilistic EEG inverse solution literature one of the most used statistical estimate is the *maximum a posteriori* estimate (MAP). Given the posterior probability density $P(x|\vec{V})$, the MAP estimate satisfies

$$x_{MAP} = \arg\max P(x|\vec{V}), \tag{4.1}$$

provided that such maximizer exist. Single point MAP estimation leads to an optimization problem and is in fact equivalent to derive a Bayesian linear inverse operator [13] B which can be formulated as:

$$B = (\vec{V}^T \Sigma^{-1} \vec{V} + R^{-1})^{-1} \vec{V}^T \Sigma^{-1} \tag{4.2}$$

where R is the covariance matrix of a prior current distribution, Σ is the covariance matrix of additive noise and $\vec{V}$ is the measured EEG potentials. Solving EEG inverse with

single point Bayesian MAP estimation is an imaging approach as we saw in Chapter 2 and produce only a single "best" solution.

To compute posterior quantities, the ideal method is surely the exact numerical evaluation. By direct numerical evaluation, we mean integration over the space $\mathbb{R}^n$ where the posterior density is defined:

$$x_f = \int_{\mathbb{R}^n} f(x)p(x|\vec{V})dx \tag{4.3}$$

of some function $f(x)$ with respect to the posterior distribution. For example, if $f(x) = x$, Eq. 4.1 becomes the formula for the *conditional mean* (x_{CM}) estimation. We could also consider the *Bayesian credibility set* which is an interval estimation to answer the question like: "In what interval are the values of x with 90 % probability, given $\vec{V}$ and prior $p(x)$? ". It still requires integration over $\mathbb{R}^n$.

Our source localization problem can be categorized into a high dimensional problem. For example, if $N = 5$ dipoles, we have 5×3 locations and moments parameters to estimate, including the number of dipoles, the number of total unknown parameters, namely the dimension of the problem is 31. In this study we work only with instantaneous EEG data. In case of spatiotemporal source localization, temporal parameters will be included into the probabilistic model and the dimension will increase dramatically. An $m-$point quadrature rule working on a $n-$dimensional posterior distribution requires m^n integration points. For example the integration of the equation Eq. at 10 points requires 31^10 operations. It is clear that this will exceed the computational capacity of computers.

An alternative way to look at the problem is the following. Instead of evaluating the probability density at given points, let the density determine a set of points, a *sample*, that supports well the distribution. These sample points can then be used for approximate integration. The most commonly used sampling technique for probability distributions is MCMC method. MCMC is essentially a *Monte Carlo integration* procedure in which the random samples are produced by evolving a *Markov chain*.

4.1.1 Monte Carlo Integration

Suppose that we want to compute a complex integral

$$\int_{\mathbb{R}^n} h(x)dx \tag{4.4}$$

If we can decompose $h(x)$ into the production of a function $f(x)$ and a probability density function $p(x|\vec{V})$ as in our case, then note that

$$\int_{\mathbb{R}^n} h(x)dx = \int_{\mathbb{R}^n} f(x)p(x|\vec{V})dx = E_{p(x)}[f(x)] \tag{4.5}$$

so that the integral can be expressed as an expectation of $f(x)$ over the density $p(x|\vec{V})$. Thus, if we draw a large number $x_1, \ldots, x_n$ of random variables from the density $p(x|\vec{V})$, then

$$E_{p(x)}[f(x)] \approx \frac{1}{n}\sum_{i=1}^{n} f(x_i) \tag{4.6}$$

This is referred to as Monte Carlo integration. By the strong law of large numbers,

$$\lim_{n\to\infty} \frac{1}{n}\sum_{i=1}^{n} f(x_i) = \int_{\mathbb{R}^n} f(x)p(x|\vec{V})dx. \tag{4.7}$$

In general, drawing independent samples from $p(x|\vec{V})$ (direct sampling) is not feasible, since the density $p(x|\vec{V})$ can be quite non-standard. In this case, it is possible to sample iteratively in such a way that at each step of the process we except to draw from a distribution that become closer and closer to $p(x|\vec{V})$. One way of doing this is through a Markov chain having $p(x|\vec{V})$ as its stationary distribution.

4.1.2 Markov Chains

Markov chain is a sequence of random variables(r.v.), $\{x_0, x_1, x_2, \ldots\}$, in which the r.v., x_{t+1}, of the next state is sampled from a distribution $p(x_{t+1}|x_t)$ which depends only on the current state of the chain x_t. That is, given x_t, the next state x_{t+1} does

not depend further on the history of the chain $\{x_0, x_1, \ldots, x_{t-1}\}$.

A particular chain is defined most critically by its *transition kernel*, $P(i,j) = P(i \to j)$, which is the probability that a process at state space s_i moves to state s_j in a single step

$$P(i,j) = P(i \to j) = Pr(x_{t+1} = s_j |\, x_t = s_i). \tag{4.8}$$

Subject to regularity conditions, the chain will forget its initial state and will converge to a unique stationary distribution, $\phi(.)$, after a sufficiently long burn-in period of m iterations. Thus as t increases, the sampled points $\{x_t\}$ will look increasingly like dependent samples from $\phi(.)$. The output of the chain can be used as in Eq. 4.9 to estimate $E[f(x)]$ where x has distribution $\phi(.)$

$$E[f(x)] = \frac{1}{n-m} \sum_{t=m+1}^{n} f(x). \tag{4.9}$$

The problem is to construct a Markov chain such that its stationary distribution $\phi(.)$ is precisely, our distribution of interest $p(x|\vec{V})$.

4.2 MCMC methods

4.2.1 The Metropolis-Hastings Algorithm

A Markov chain with a stationary distribution $p(x|\vec{V})$ can be constructed by using Metropolis-Hastings algorithm [35] which is a generalization of the method first proposed by Metropolis *et al.* [36].

For the Metropolis-Hastings algorithm, at each iteration t, the next state x_{t+1} is chosen by first sampling a candidate point x^* from a proposal distribution $q(.|x_t)$.

The candidate point x^* is then accepted with probability $\alpha(x_t, x^*)$ where

$$\alpha(x_t, x^*) = \min(1, \frac{p(x^*|\vec{V})q(x|x^*)}{p(x|\vec{V})q(x^*|x)}). \tag{4.10}$$

If the candidate is accepted, the next state becomes $x_{t+1} = x^*$. If the candidate is rejected, the chain does not move, $x_{t+1} = x_t$. With any reversible proposal distribution the stationary distribution of the chain will be $p(x|\vec{V})$. The transition kernel for the Metropolis-Hastings algorithm is

$$P(x_{t+1}|x_t) = q(x_{t+1}|x_t)\alpha(x_t, x_{t+1}) + I(x_{t+1} = x_t)[1 - \int q(x^*|x_t)\alpha(x_t, x^*)dx^*] \tag{4.11}$$

where $I(.)$ denotes the indicator function that takes the value 1 when the argument is true, and 0 otherwise. The first term in Eq. 4.11 arises from the acceptance of candidate and the second term from rejection. Using the fact that

$$p(x_t|\vec{V})q(x_{t+1}|x_t)\alpha(x_t, x_{t+1}) = p(x_{t+1}|\vec{V})q(x_t|x_{t+1})\alpha(x_{t+1}, x_t) \tag{4.12}$$

which follows from Eq. 4.10, the *detailed balance equation*, a sufficient condition for a unique stationary distribution is obtained:

$$p(x_t|\vec{V})P(x_{t+1}|x_t) = p(x_{t+1}|\vec{V})P(x_t|x_{t+1}) \tag{4.13}$$

Integrating both sides of Eq. 4.13 with respect to x_t gives:

$$\int p(x_t|\vec{V})P(x_{t+1}|x_t)dx_t = p(x_{t+1}|\vec{V}) \tag{4.14}$$

In Metropolis-Hastings algorithm it is assumed that the unknown parameter vector x is a fixed-length vector. However, in this EEG inverse formulation, N, the number of active dipoles is assumed to be unknown so that the dimension of x is variable, namely EEG inverse formulation also includes a model selection problem. This considerably extends the scope of Metropolis-Hastings algorithm. In order to sample without prior determination of the number of dipoles, a trans-dimensional sampling strategy is needed.

4.2.2 The Independence Sampler

The most straightforward MCMC approach that can allow moves between spaces of different dimensions is the *independence sampler* (IS). For the IS, the proposal distribution does not depend on the current values: $q(x_{t+1}|x) = q(x_{t+1})$. So, subsequent iterations can generate independent candidates of varying dimensions. The acceptance probability in Eq. 4.10 is

$$\alpha(x_t, x^*) = \min(1, \frac{p(x^*|\vec{V})q(x)}{p(x|\vec{V})q(x^*)}). \tag{4.15}$$

It is known that the IS works best if the proposal q is a reasonable approximation to the target posterior distribution which is clearly difficult to achieve.

In our experience, a straightforward implementation of the MCMC technique was likely to fail in EEG source reconstruction problem. This was determined by generating multiple independence sampler runs with different starting points and random seeds. The results of the IS when proposal distributions for dipole parameters at each iteration are independent and uniform are shown in Chapter 5, Table 5.2. IS requires tremendous time to explore the whole range of parameter space and suffers from slow convergence problem.

4.2.3 Reversible Jump MCMC

The independence sampler is unlikely to represent the best strategy. Therefore, it seems sensible to allow the proposal distributions to depend on the current values. Peter J.Green developed reversible jump MCMC (RJMCMC) for model determination problems in 1995 [37]. RJMCMC is a framework for the construction of reversible Markov chain samplers that can jump between parameter subspaces of differing dimensionality in a flexible way, while retaining detailed balance which ensures the correct limiting distribution.

If location and moment parameters, $\vec{r}$ and $\vec{m}$ are combined in a parameter set θ, each state x_i of our reversible chain will be composed of two components, $x_i = (N_i, \theta_i)$ where N_i,the number of dipoles, is the model indicator and θ_i is the dipole parameters. In RJMCMC paradigm, the move from (N_i, θ_i) to (N_{i+1}, θ_{i+1}) is proposed by drawing a random parameter set U_i and setting $\theta_{i+1} = f_{N_i \to N_{i+1}}(\theta_i, U_i)$. $f_{N_i \to N_{i+1}}$ is a deterministic function that defines the mapping between the parameter spaces. When considering a move from the state (N_i, θ_i) to (N_{i+1}, θ_{i+1}) and the reverse move from (N_{i+1}, θ_{i+1}) to (N_i, θ_i), the vectors of the Markov chain states and proposal random variables (θ_i, U_i) and (θ_{i+1}, U_{i+1}) must be of equal dimension. That is the dimension matching condition

$$dim(\theta_i) + dim(U_i) = dim(\theta_{i+1}) + dim(U_{i+1}). \tag{4.16}$$

In our design, a move from (N_i, θ_i) to (N_{i+1}, θ_{i+1}) is proposed in two steps. First step is to generate a new model indicator N_{i+1} from the proposal distribution q^{ind} where $q^{ind}(N_{i+1}|N_i)$ is the probability of the jump from the model N_i to N_{i+1}. Given a model indicator, N_{i+1}, the second step is to generate dipole parameters of the dimension N_{i+1} from the proposal distribution q^{par}. Subscripts *ind* and *par* are labels for model indicator and dipole parameters respectively. In our sampling procedure, a candidate sample (N_{i+1}, θ_{i+1}) is chosen with three categorized moves:

- **Perturbation move**: if $N_{i+1} = N_i$

  Location and magnitude parameters are updated by proposal distribution q^{par}. The location parameter $\vec{r}_{i+1}$ is sampled from the proposal distribution $q^{par}_{\vec{r}_{i+1}}$, a Gaussian density centered on $\vec{r}_i$ (the location parameter of the previous state) with standard deviation $\sigma_{loc} = 8mm$. For the magnitude parameters, $q^{par}_{\vec{m}_{i+1}}$ is a Gaussian density centered on $\vec{m}_i$ with standard deviation $\sigma_m = 10nAm$. Since this jump is between two models of equal dimension, this move is a straightforward implementation of simultaneous Metropolis-Hastings algorithm.

- **Trans-dimensional moves**: if $N_{i+1} \neq N_i$

  - Birth move: $(N_{i+1} - N_i)$ new dipole(s) and its parameters are randomly

proposed, $\theta_{i+1} = (\theta_i, U)$ where $dim(U) = (N_{i+1} - N_i)$. The proposal distribution for U is uniform over the location and magnitude spaces and does not depend on the previous values as in the independence sampler.

– Death Move: $(N_i - N_{i+1})$ randomly chosen dipole(s) is proposed to be removed.

The acceptance probability for the RJMCMC algorithm is stated as:

$$\alpha_{RJ} = min\left\{1, \frac{p(N_{i+1}, \theta_i \mid \vec{V})\ q^{ind}(N_i|N_{i+1}) q^{par}(\theta_i|\theta_{i+1})}{p(N_i, \theta_i|\vec{V}) q^{ind}(N_{i+1}|N_i) q^{par}(\theta_{i+1}|\theta_i)} \left|\frac{\partial f_{N_i \to N_{i+1}}(\theta_i, U_i)}{\partial(\theta_i, U_i)}\right|\right\} \quad (4.17)$$

The Jacobian appears due to the use of deterministic transformation in proposal mechanisms and not an inherent component of MCMC induced dimension changed. In random birth and death moves, $f_{N_i \to N_{i+1}}$ is set to identity: $\theta_{i+1} = (\theta_i, U_i)$, the Jacobian of the transformation is equal to 1.

4.3 Strategies for Improving Reversible Jump MCMC

The posterior distribution $p(x|\vec{V})$ has numerous valleys and peaks over the solution space, namely high probability areas are separated by regions of very low probability. For such multimodal distributions, MCMC can be prone to entrapment in local optima; a Markov chain currently exploring a peak of high probability may experience difficulty crossing valleys to explore other peaks. A properly constructed Markov Chain will eventually cross even very deep valleys in the posterior probability distributions of dipole parameters. However, it may take a prohibitive amount of time to adequately explore a rough volume of dipole parameters. As a result, a large number of parameters may go unexplored in a standard MCMC analysis.

4.3.1 Simulated Annealing

One approach to escape local optima is based on an additional parameter called *temperature* that changes the probability of moving from one point of the search space to another. Simulated annealing (SA) is a well-known heuristic technique that mathematically mirrors the cooling of a set of atoms to a state of minimum energy [38]. The idea is that when we initially start sampling the space, we will accept a reasonable probability of a move from a higher probability state to a lower probability state in order to explore the entire solution space. As the SA proceeds, the probability of such "down-hill moves" is decreased.

SA is very closely related to Metropolis sampling, differing only in that the probability α in Eq. 4.10, such that

$$\alpha_{SA}(x_t, x^*) = \min\left(1, \frac{p(x^*|\vec{V})q(x|x^*)}{p(x|\vec{V})q(x^*|x)}\right)^{\frac{1}{T(t)}} \tag{4.18}$$

where the function $T(t)$ is called the cooling schedule.

SA coupled RJMCMC algorithm designed for EEG source reconstruction process is shown in Figure 4.1. In our algorithm the cooling schedule is exponential cooling which is generally accepted as the best schedule [39]:

$$T(t) = T_0(\frac{T_f}{T_0})^{\frac{t}{n}} \tag{4.19}$$

where $T_0 = 100$ is the initial temperature,$T_f = 1$ is the final temperature, and n is the total iteration number. Setting $T = 1$ recovers RJMCMC algorithm.

4.3.2 Parallel Tempering

In parallel tempering coupled RJMCMC method (PT-RJMCMC), instead of constructing a single Markov chain, k Markov chains $C_i = (x_i^{(1)}, \ldots, x_i^{(n)})$, $i = 1, \ldots, k$, are simultaneously run on the dipole parameter space. Each chain is associated with a

SA-RJMCMC Algorithm

Begin

i=0

Initialize a random dipole number, N_i, from $U(N_{min},N_{max})$

Initialize a random dipole configuration, θ_i

Evaluate $p(N_i,\theta_i|V)$

$T=T_{max}$

while ($T \geq T_{min}$)

for i=1 to k

Pick a dipole number N_{i+1} from $q^{ind}(N_{i+1} \mid N_i)$

if $N_{i+1}=N_i$ → **Perturbation Move**

Simultaneous Metropolis Hastings

$\theta_{i+1}= q^{par}(\theta_i, rand(U))$ where $dim\ (U_{i+1 \to i}) = N_{i+1}= N_i$

elseif $N_{i+1}<N_i$ → **Death Move**

Pick $(N_i - N_{i+1})$ random dipole parameter from θ_i and destroy

Update θ_i

$\theta_{i+1}= q^{par}(\theta_i, rand(U))$ where $dim\ (U_{i+1 \to i})=(N_i - N_{i+1})$

elseif $N_{i+1}>N_i$ → **Birth Move**

Indepence Sampler for $(N_{i+1} - N_i)$ dipole parameter

Single Component Metropolis Hastings for (N_i) dipole parameter

$\theta_{i+1}= q^{par}(\theta_i, rand(U))$ *where* $dim\ (U_{i+1 \to i})=(N_{i+1} - N_i)$

end

Evaluate $p(N_i,\theta_i|V)$

Accept (N_i,θ_i) with probability $\alpha_{SA\text{-}RJMCMC}$

$$\alpha_{SA\text{-}RJMCMC} = \min\left\{1, \frac{p(N_{i+1},\theta_i \mid V)\, q^{ind}(N_i|N_{i+1}) q^{par}(\theta_i|\theta_{i+1})}{p(N_i,\theta_i|V) q^{ind}(N_{i+1}|N_i) q^{par}(\theta_{i+1}|\theta_i)} \left|\frac{\partial q^{par}_{i+1\to i}(\theta_i,U)}{\partial(\theta_i,U)}\right|^{1/T}\right\}$$

Update $T=\beta T$

end while

End

Figure 4.1 SA coupled RJMCMC algorithm for EEG source reconstruction.

temperature parameter T_i such that $T_i = 1$ and $T_i < T_{i+1}$. The stationary distribution of C_i is

$$\phi_i = p_i(N, \theta|\vec{V})^{\frac{1}{T_i}}. \tag{4.20}$$

In this way, hot chains are associated with probability distributions that come closer and closer to the limiting case of $T = \infty$, in which case the associated density is constant. As temperature increases, deep valleys and local modes are smoothed out, and the corresponding distribution become easier to sample.

After each iteration an attempt is made to swap the dipole parameters of two randomly chosen contiguous chain C_i and C_{i+1}. The probability of accepting the proposed swap is

$$\alpha_{PT} = min\left(1, \frac{p_i(N^{i+1}, \theta^{i+1}|\vec{V})p_{i+1}(N^i, \theta^i|\vec{V})}{p_i(N^i, \theta^i|\vec{V})p_{i+1}(N^{i+1}, \theta^{i+1}|\vec{V})}\right). \tag{4.21}$$

The idea behind this PT move is that the hot chains will make a fast but unspecific exploration of the dipole parameter space without getting trapped in local modes. The PT move allows them to feed in high probability values to the colder chains, going ultimately down to the principal chain C_1 that samples the posterior. At the end of the run, output from the modified chains with $T > 1$ are discarded.

For the current EEG source reconstruction problem, PT method affords significant improvement over SA as shown in Chapter 5.

4.4 Convergence Diagnostics

Before the samples obtained from the MCMC sampling are from the equilibrium distribution they cannot be used in source reconstruction. To estimate how much the inference based on MCMC simulations differs from the desired target distribution $p(N, \theta|\vec{V})$, a convergence diagnostic called *potential scale reduction factor* (PSRF),

(also called Gelman-Rubin) test is used [34].

The general approach for monitoring convergence is to run multiple parallel simulations with overdispersed starting points and to check if the iteration number was large enough for the Markov Chain to "forget" where it started. The usual method is to plot chains' outputs and compare to them qualitatively. However, the number of iterations needed to reach the equilibrium can be approximated using the output of the simulation by using PSRF test.

PSRF test implemented in this study, estimates when two or more sample chains started from different points are from the same distributions by comparing the between-chain variation and within-chain variation. Assume that estimated values for each dipole parameter at each iteration are obtained after the run m Markov chain simulations of length n. Let us label a single dipole parameter as ψ and ψ_{ij} as the output of the j^{th} chain's i^{th} iteration. Between-chain variance σ_B^2 is

$$\sigma_B^2 = \frac{n}{m-1}\sum_{i=1}^{m}(\overline{\psi}_{i.} - \overline{\psi}_{..}), \tag{4.22}$$

where

$$\overline{\psi}_{i.} = \frac{1}{n}\sum_{j=1}^{n}(\psi_{ij}), \qquad \overline{\psi}_{..} = \frac{1}{m}\sum_{i=1}^{m}(\overline{\psi}_{i.}), \tag{4.23}$$

and within-chain variance σ_W^2 is

$$\sigma_W^2 = \frac{1}{m}\sum_{i=1}^{m} s_i^2, \tag{4.24}$$

where

$$s_i^2 = \frac{1}{n-1}\sum_{j=1}^{n}(\psi_{ij} - \overline{\psi}_{i.})^2. \tag{4.25}$$

From these two variance components, σ^2, the variance of the dipole parameter ψ can be estimated as

$$\hat{\sigma^2} = \frac{n-1}{n}\sigma_W^2 + \frac{1}{n}\sigma_W^2 \tag{4.26}$$

which is an unbiased estimate of the true variance σ^2 , if the starting points of the sequences were drawn from the target distribution. The PSRF $\hat{R}$ is given by the comparison of $\hat{\sigma^2}$ and within-chain variance,

$$\hat{R} = \frac{\hat{\sigma^2}}{\sigma_W^2}. \tag{4.27}$$

If R is not near 1 for all elements of the dipole parameter set, the results are rejected. The simulation length is updated to the estimated effective number of iterations, $n^{eff} = n\hat{R}$.

4.5 Current Density Map Generation

The next step after sampling a posterior distributions of active dipole number, location and moments, is to form the current density maps.

At each MCMC iteration dipole parameters were fitted to the data with an ECD approach as the upper limit for the number of the active dipole (N_{max}) is much less than the number of predefined set of dipoles (N_v). To pass from the isolated source model to the imaging approach, firstly the active dipole number with maximum a posterior probability (MAP) is found. From the chain history, dipole location and moment parameters belonging to the dipole parameter set with $N = N_{MAP}$ are chosen. The ℓ_2-norm of the 1×3 moments vector $\vec{m}$, gives the magnitude M of this dipole. Finally, to generate the relative strength for each location, we use the formulation:

$$J_i = \{p(\vec{r_i})M_i| \;\; p_i(M_i) = \max(p_i(M)\}. \tag{4.28}$$

where J_i is the magnitude of the relative strength of the i^{th} candidate dipole source; $p(\vec{r_i})$ shows the probability of existing an active source at its location, and M_i is the magnitude assigned to this dipole with MAP probability.

5. EVALUATION OF THE BAYESIAN MCMC METHOD: SIMULATED DATA

Theoretical approach presented in chapter 3 and 4 is firstly applied on simulated EEG data. We used realistic instantaneous EEG simulation data corrupted with Gaussian noise of zero mean and standard deviation σ_E. Except where otherwise noticed, σ_E is chosen to obtain a signal-to-noise ratio (SNR) of 10dB. At each trial noise covariance vector Σ is estimated by $n = 150$ random noise realizations with Eq. 5.1

$$\Sigma = \frac{1}{n} \sum_{i=1}^{n} \left(\vec{E}_i - \vec{E}_m \right) \left(\vec{E}_i - \vec{E}_m \right)^T \tag{5.1}$$

where $\vec{E}_i$ is the i^{th} noise vector; $\vec{E}_m$ is the mean of all realizations.

Localization error in each trial is computed as

$$LE = \|\vec{r}_e - \vec{r}_o\| \tag{5.2}$$

where $\vec{r}_e$ is the estimated location and $\vec{r}_o$ is the original location coordinates.

5.1 Simulation and Solution Space

EEG simulations are produced by solving the forward problem using Boundary Element Method (BEM) with center of gravity (COG) approximation on a realistic head model. Realistic head model consists of brain, skull and scalp surfaces. Surfaces of the brain, skull and scalp are tesselated with 2000, 1200 and 1200 triangles, respectively.

Instantaneous EEG inverse problem is solved on the model developed from the T1 weighted average head image issued by the Montreal Neurological Institute (MNI)[6]. 3-D segmentation of the brain, skull and scalp are made using Statistical Parametric Mapping software 99 (SPM99) developed by Wellcome Institute [40]. 30 channel electrode locations (Fp1, Fp2, F7, F3, Fz, F4, F8, FT7, FC3, FCz, FC4, FT8,

T7, C3, Cz, C4, T8, TP7, CP3, CPz, CP4, TP8, P7, P3, Pz, P4, P8, O1, Oz, O2) are registered to the scalp surface by spline interpolation using the T1 weighted MR data, the inion-nasion and pre-auricular coordinates, and the 10-20 Electrode Placement System.

The solution space contains 1360 voxel as candidate dipole locations, distributed throughout the gray matter volume of the brain. The spatial resolution of the head model is **8mm**.

This way, the simulation and solution space have different discretization so that the most common *crime* in inverse estimation, which is defined as using exactly the same model for the simulation and the reconstruction [41], was avoided.

5.2 Comparison of MCMC Methods for EEG Source Reconstruction

5.2.1 Reversible Jump MCMC versus Independence Sampler

Our first study was to compare the performance of the RJMCMC algorithm with that of IS. The dipole source used to generate the measurements of this simulation study is located at the Brodmann area (BA)17, with a dipole magnitude of 10nAm. Source localization results of RJMCMC and IS are shown in Table 5.1 and Table 5.2, respectively.

The RJMCMC sampler was distinctly superior to IS which suffers from slow convergence problem. However, even though RJMCMC gives more accurate results comparing to IS, without coupling it with an heuristic, it is prone to "getting stuck" on local optima.

Table 5.1
RJMCMC source localization results. Original dipole location=[-16 -94 -34]. IN= Iteration Number, EDN= Estimated Dipole Number, EDL= Estimated Dipole Location, LE=Localization Error.

	IN	EDN	EDL	LE
Simulation 1	1000	1	[-16 -94 -10]	24mm
Simulation 2	1000	1	[8 -94 -26]	24mm
Simulation 3	2000	1	[-16 -94 -10]	24mm
Simulation 4	2000	1	[8 -94 -26]	24mm
Simulation 5	3000	1	[8 -94 -26]	24mm
Simulation 6	5000	1	[8 -94 -26]	24mm
Simulation 7	10000	1	[-16 -86 -34]	8mm
Simulation 8	20000	1	[-8 -94 -34]	8mm
Simulation 9	50000	1	[-16 -94 -34]	0mm
Simulation 10	50000	1	[-16 -94 -34]	0mm

Table 5.2
Independence sampler source localization results. Original dipole location=[-16 -94 -34].

	IN	EDN	EDL	LE
Simulation 1	10000	1	[16 -46 -66]	66mm
Simulation 2	10000	1	[24 -62 -66]	60.3mm
Simulation 3	10000	1	[-8 -86 -18]	19.5mm
Simulation 4	10000	1	[-24 -62 -58]	40.7mm
Simulation 5	20000	2	[8 -94 -34] [-32 -46 38]	102mm
Simulation 6	20000	1	[8 -94 -26]	24mm
Simulation 7	50000	1	[-16 -94 -34]	0mm
Simulation 8	50000	1	[0 -94 -34]	16mm
Simulation 9	100000	1	[-16 -94 -34]	0mm
Simulation 10	100000	1	[8 -94 -26]	24mm

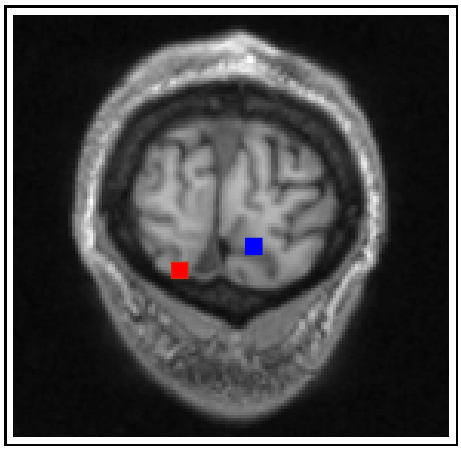

Figure 5.1 Coronal view of the occipital cortex. The dipole located at the BA 17 is shown in red and the dipole located at the BA 18 is shown in blue. The blue dipole acts like a local optimum so that sampler risks to be trapped in that location when sampling dipole parameters for the EEG data produced by the red dipole.

5.2.2 SA versus Parallel Tempering

While sampling dipole parameters from the posterior distribution given the EEG data produced by the activation of a dipole source located at the **BA 17**, a dipole at the **BA 18** (coordinates: [8 -94 -26]) acts like a local optimum. Without the help of heuristics RJMCMC sampler has a tendency to getting stuck in that location. These dipoles are shown in Figure 5.1.

The implementation of SA and PT heuristics affords significant improvement in the source localization results as shown in Table 5.3. PT coupled RJMCMC is capable of escaping the local optima and can find the accurate location within 10000 iterations. The results of a PT-RJMCMC run are shown in Figure 5.2.

5.3 Evaluation of the Bayesian PT-RJMCMC

Intensive simulation studies are done in order to further investigate the feasibility of the PT-RJMCMC sampling method. We tested our approach with four different dipole configuration scenarios. Our hybrid PT-RJMCMC algorithm were run with five chains, for 10000 iterations. For each data, we conducted five runs with different

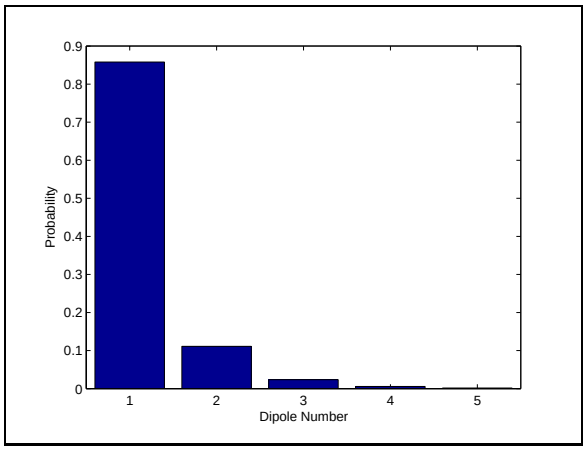

(a) Posterior distribution for dipole number.

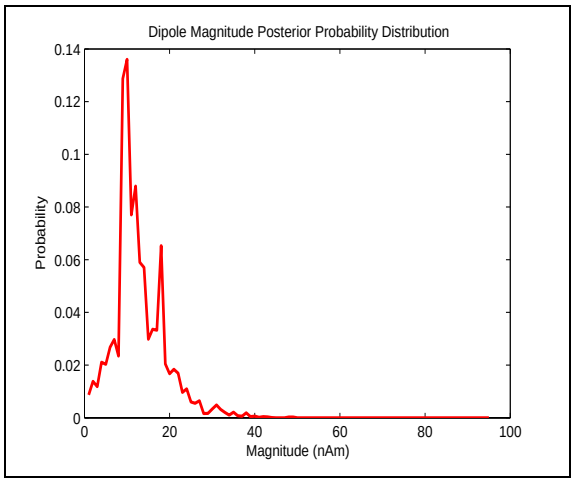

(b) Posterior distribution for dipole magnitude.

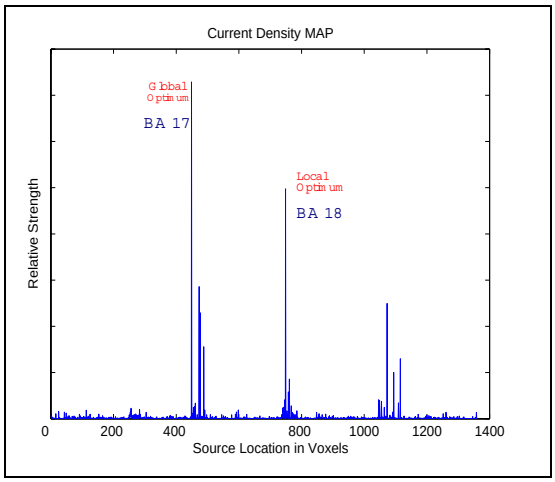

(c) Current density map.

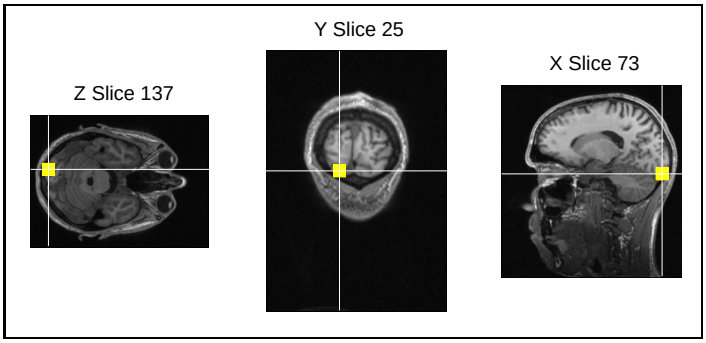

(d) Current density map projected on the MR volume.

Figure 5.2 PT-RJMCMC source reconstruction results. EEG data is produced by the activation of a single dipole locating at the BA 17. The dipole magnitude is 10 nAm. (a) shows posterior probability of the dipole number, (b) posterior probability for dipole magnitude, (c) current density map and (d) source localization results in the realistic head model.

Table 5.3
A total of 75 MCMC runs were tested to compare SA and PT methods. Using PT results in a significant reduction of local optima errors. LO= Local Optima, LE=Localization Error.

Method	Number of Iterations	Number of Chains	RJMCMC runs stuck in a LO	Mean LE
RJMCMC	25000	1	10	4.8mm
SA-RJMCMC	25000	1	7	3.36mm
PT-RJMCMC	10000	5	0	0mm

random seeds to check the consistency of results. To monitor the convergence, we used the PSRF test and for R values greater than 1.1, simulation results were rejected. First 25% of iterations were discarded for each chain as the burn-in period. The active dipole number was assumed to be unknown and we did not used any specific a prior distribution for location and magnitude parameters. Prior distributions for dipole parameter set x were:

- N: Uniform between $N_{min} = 1$ and $N_{max} = 5$,
- $\vec{r}$: Uniform over 1360 predefined voxels,
- $\vec{m}$: Uniform between $m_{min} = -200nAm$ and $m_{max} = 200nAm$. The negative sign means that the dipole orientation is reversed.

In Chapter 2, it is stated that a patch of $5mm \times 5mm \times 4mm$ in the cortex produce a net current of 10nAm. In the current model, a voxel has a volume of $8mm \times 8mm \times 8mm$ and can produce approximately a net current of $50nAm$. Hence, these limitations permit stronger and weaker neural activity; even the deepest dipole with lowest values at the transfer function K can produce potentials up to $120\mu V$.

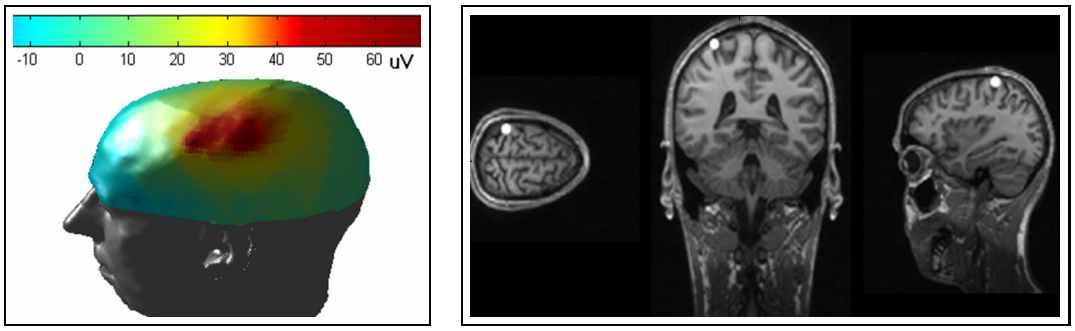

(a) Scalp topography. (b) Source location.

Figure 5.3 Exemplar dipole localization result of the EEG data produced by a single superficial source.

5.3.1 Simulation A: Single Superficial Source

We simulated realistic EEG data produced by single sources located at the cortex surface. The inverse problem is solved for 43 different EEG data sets produced by dipoles at different locations with low or high magnitude. Inverse method has correctly detected sources and no localization error has been found.

Figure 5.3 shows localization result and scalp topography for EEG produced by the exemplar dipole located at [-32 -22 54] MNI coordinates.

During our analysis, we detected two dipoles at different locations and magnitudes but producing exactly the same EEG data. This EEG data are localized by PT-RJMCMC method and multiple signal decomposition algorithm (MUSIC). MUSIC has only detected one of these dipoles. However, PT-RJMCMC resulted in a probability function peaking at these two dipoles and showed the ambiguity of the problem. Figure 5.4 shows the localized dipoles and MCMC results.

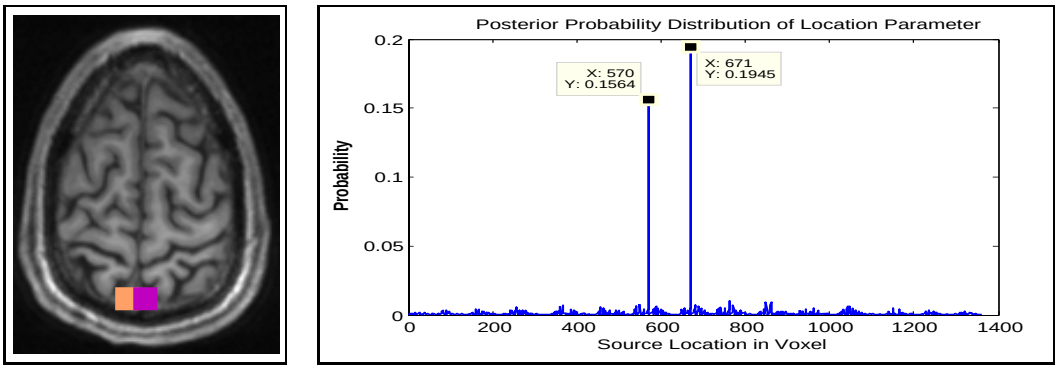

(a) Dipole Locations. (b) Posterior dipole location probability distribution.

Figure 5.4 Dipole 570 at [-8 -62 54] and dipole 671 at [0 -62 54] generate the same EEG potentials. This figure represents (a) dipole locations, (b) PT-RJMCMC dipole analysis results.

5.3.2 Simulation B: Single Deep Source

One of the problems in dipole source localization is *depth biasing*: The underestimation of deep sources in favor of more superficial ones, leading to solutions that tend to explain the data with the generators near the sensors [42]. The method was tested on 345 sources, away from surface and electrodes, to test its ability of locating the deep sources. The simulation results in **0.46mm** mean localization error. Localized dipole sources are shown in Figure 5.5.

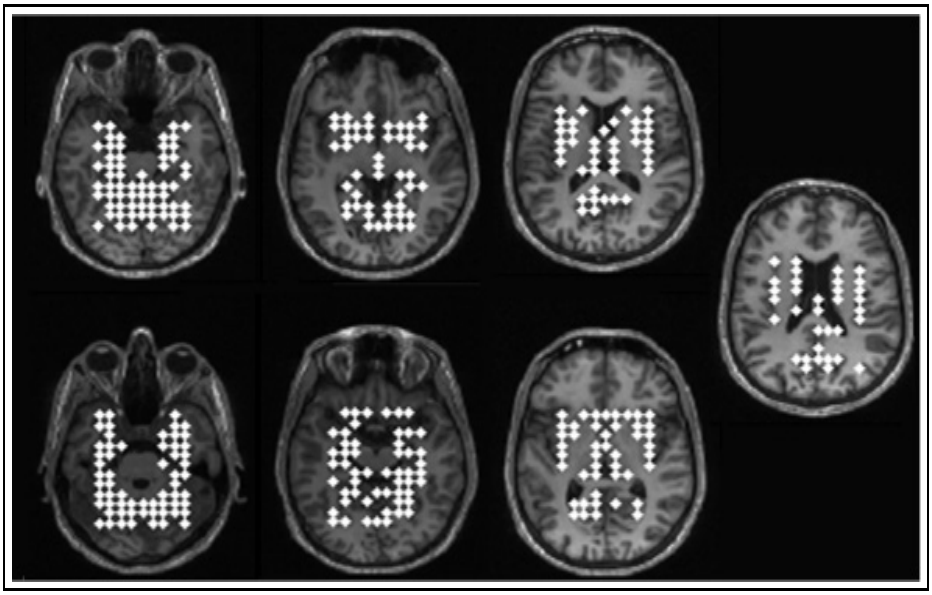

Figure 5.5 Localized deep dipole sources.

5.3.3 Simulation C: Two Uncorrelated Sources

We considered in this section the case of two simultaneously active sources set of equal or different strength. 50 dipole pairs from different hemispheres, producing spatially uncorrelated EEG potentials were selected. Figure 5.6 shows EEG potentials and scalp topography produced by the activation of two distant sources and Figure 5.7 shows PT-RJMCMC localization results.

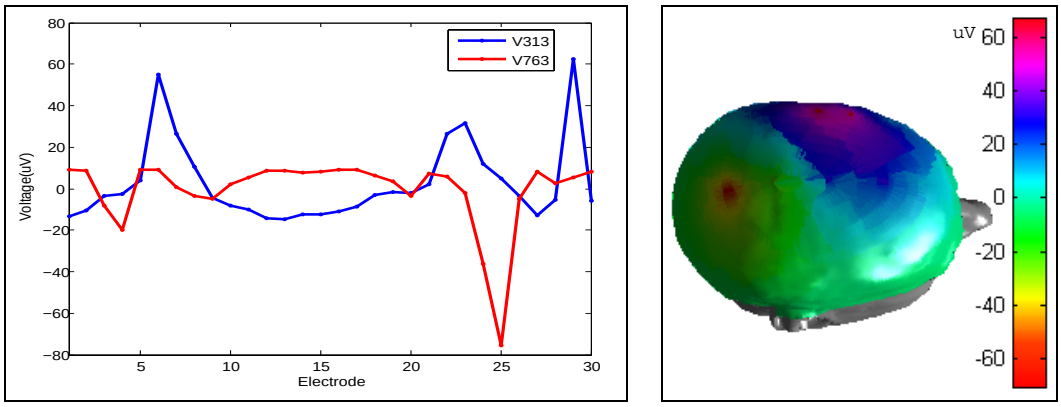

(a) EEG Potentials. (b) Scalp topography.

Figure 5.6 Potentials produced by two dipoles, total $\vec{V} = \vec{V}_{313} + \vec{V}_{763}$.

Table 5.4
Sample results from simulation C. $\vec{r_o}$ is the original location, M_o is the original magnitude,$\vec{r_e}$ is the estimated location and M_e is the estimated magnitude of sources.

$\vec{r_o}$	M_o(nAm)	$\vec{r_e}$	M_e(nA-m)
[-32 2 54]	21	[-32 -6 54]	20
[8 -62 54]	19	[8 -62 54]	17.5
[-32 -22 6]	20	[-32 -22 6]	20.7
[32 18 30]	10	[16 18 30]	12
[-64 -46 -10]	10	[-64 -46 -10]	10
[56 18 14]	2		
[-64 -46 -10]	30	[-64 -46 -10]	31
[56 18 14]	30	[56 18 14]	29

Dipole's relative power in measurement space (i.e electrodes) influence the re-

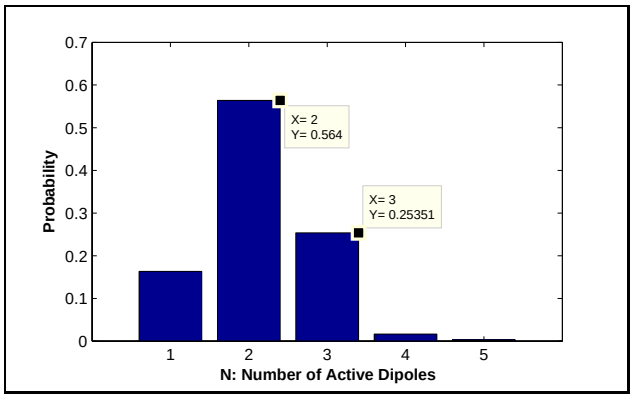

(a) Active dipole number histogram.

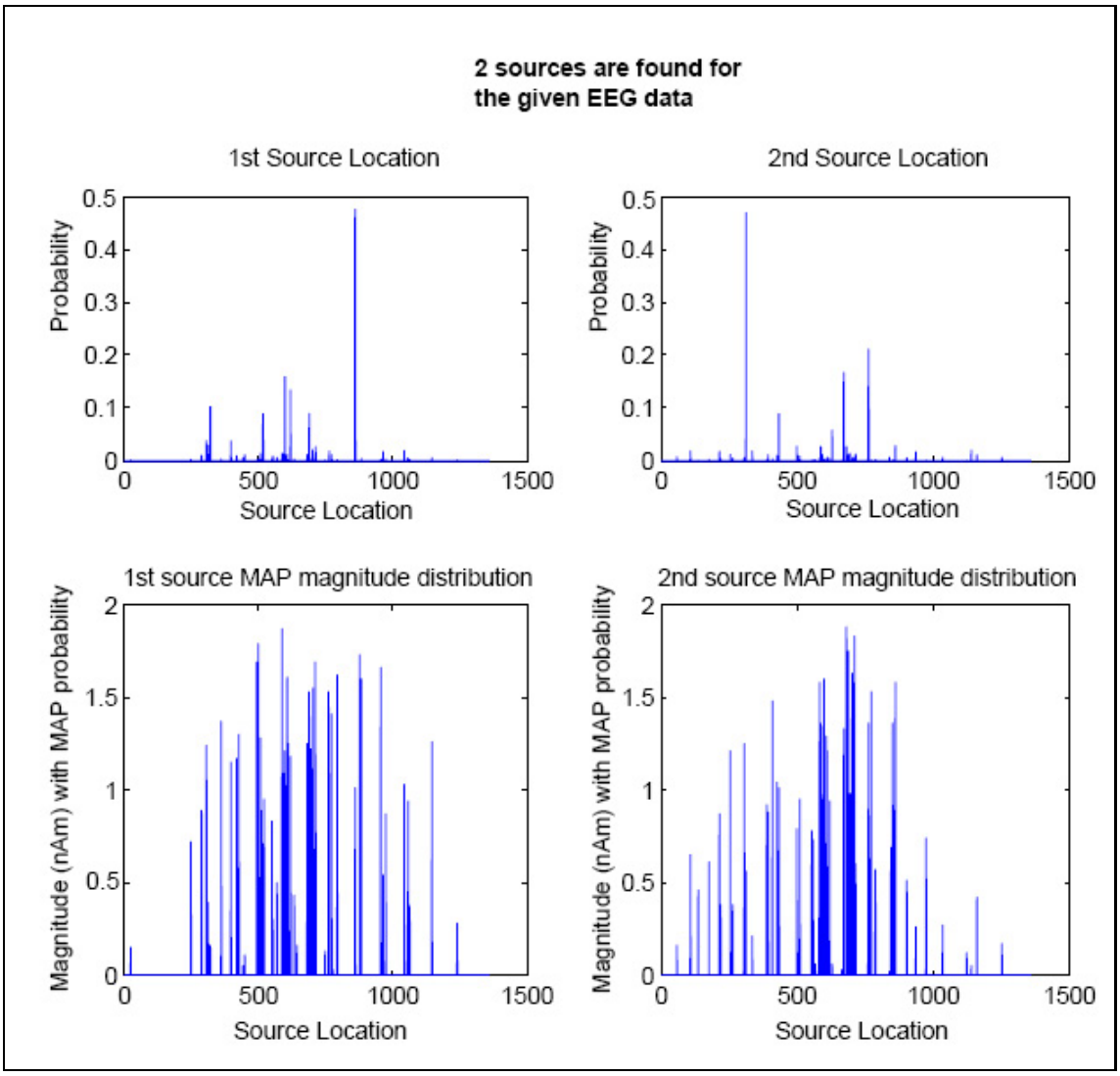

(b) MCMC source localization result.

Figure 5.7 EEG data produced by two uncorrelated dipole activity is localized by PT-RJMCMC method. Active dipole number (a) and dipole locations (b) are accurately estimated.

construction accuracy. As the dipole magnitudes and relative power were equal, the number of active dipoles was estimated correctly. In the case of high-low magnitude dipole pairs, the method finds the probability of single dipole higher as shown in Table 5.4.

5.3.4 Simulation D: Multiple Sources

The performance of the method was tested for conditions where multiple sources in the same region were active simultaneously. Sample dipole localization results are shown in Table 5.5 and Figure 5.8.

Table 5.5
Sample results from simulation D.

$\vec{r_o}$	M_o(nAm)	$\vec{r_e}$	M_e(nAm)
[8 18 54]	11	[8 18 54]	12
[16 18 54]	11	[16 18 54]	10
[-8 18 54]	11	[-8 18 54]	10
[32 10 46]	2	[24 18 46]	1.8
[32 18 30]	2	[32 18 30]	2.1
[32 18 38]	2	[32 18 38]	1.9
[32 18 46]	2	[32 18 46]	2
[-40 -30 -26]	12	[-56 -30 22]	19.5
[-40 -30 46]	10.5		
[48 -6 38]	5	[48 -6 38]	4.5
[48 -14 38]	5	[48 -14 38]	5.5

5.3.5 Localization Errors

Table 5.6 contains the localization errors of the Bayesian PT-RJMCMC method for the four different simulations.

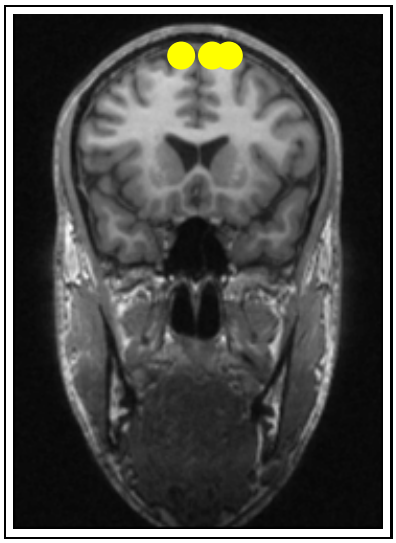

(a) Original source locations.

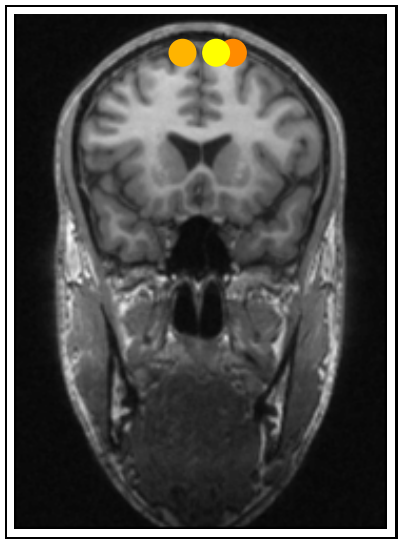

(b) Estimated source locations.

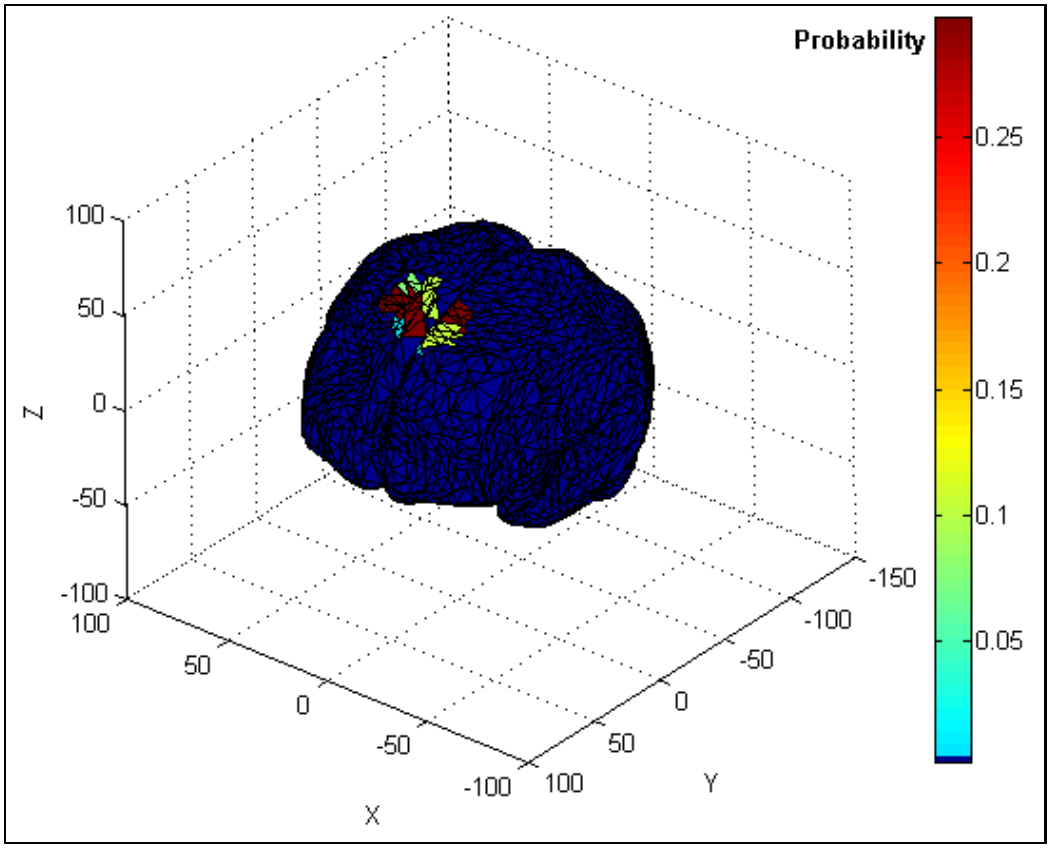

(c) Estimated source locations.

Figure 5.8 Simulated EEG data produced by three dipole sources locating at superior frontal gyrus with MNI coordinates [8 18 54], [16 18 54] and [-8 18 54] are localized. (a) shows original source locations. Dipole moments are radial to the cortex surface and magnitudes are equal (11 nAm)(b) shows source reconstruction results in the head volume and (c) on the cortex surface. Dipole locations are exactly found and magnitudes with an error of 1 nAm.

Table 5.6
Localization errors in simulation studies. SNR=10dB.

Simulation Type	Number of Trials	Correct Location within 0mm-8mm-10mm			Mean LE
Simulation A	43	100 %	100 %	100 %	0mm
Simulation B	345	95 %	98 %	100 %	0.46mm
Simulation C	50	22 %	68 %	88 %	9.76mm
Simulation D	150	20 %	70 %	90 %	7.47mm

As shown in Table 5.7 signal-to-noise ratio (SNR) is as effective as the numbers, locations and relative strength of dipoles on the performance of the method.

Table 5.7
Localization errors in mm for different SNRs.

	SNR 25dB	SNR 15dB	SNR 10dB	SNR 5dB	SNR 2dB
Simulation A	0	0	0	0.93	1.86
Simulation B	0	0	0.46	1.02	2.45
Simulation C	3.10	4.12	9.76	12.16	24.01
Simulation D	2.85	3.76	7.47	11.05	28.1

5.4 Comparison with MUSIC

As we saw in Chapter 2, MUSIC is widely accepted as an effective method in locating EEG potentials produced by focal sources. When only one dipole source is active, both MUSIC and Bayesian method give almost always the exact location even if the SNR is significantly low. However, MUSIC is a technique that searches for sources that are independent of each other in time. The results of the MUSIC procedure are misleading if several synchronously active sources are responsible for the recorded signals. When two source are synchronously active as shown in Figure 5.9, MUSIC points the "center of mass" of brain activity as the source generator whereas Bayesian

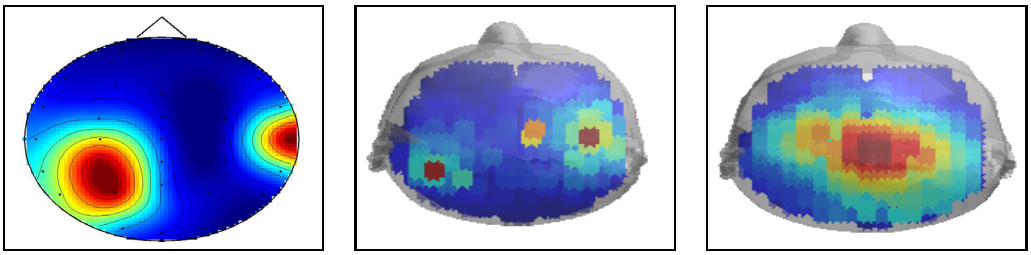

(a) Scalp map. (b) MCMC result. (c) MUSIC result.

Figure 5.9 Simulated EEG data is generated by the activity of two dipoles, locating at left parietal and right temporal lobe. (a)2D scalp topography, (b)MCMC method (c) MUSIC method source localization results projected to the head volume are represented.

method can accurately locate two sources. Sample results reflecting the effectiveness of two methods for focal type of dipole configuration are represented in Table 5.8.

Table 5.8
Source localization accuracy of Bayesian PT-RJMCMC method is compared with MUSIC for focal source activity.

Source Configuration	True Location	MCMC Result	MUSIC result
Single Superficial	[-24 10 54]	[-24 10 54]	[-24 10 54]
Single Deep	[-24 10 -42]	[-24 10 -42]	[-24 10 -34]
Two Uncorrelated	[-32 2 54] [8 -62 54]	[-32 2 54] [8 -62 54]	[-8 -22 62]
Two Correlated	[8 10 54] [8 26 54]	[8 10 54] [8 26 54]	[8 18 54]

5.5 Comparison with LORETA

LORETA method solves the EEG inverse problem based on a physiological assumption: Neighboring neuronal populations are simultaneously and synchronously activated. It is being used in clinical and cognitive studies successfully.

5.5.1 Extended Neural Activity

To compare Bayesian and LORETA inverse solutions, we produced a patch-type dipole activation locating at primary visual cortex. Dipole configuration consists of two main generators and eight neighbor dipoles with relatively low magnitude. Scalp topography produced by these ten sources is shown in Figure 5.10. Instantaneous neural activity is localized by Bayesian PT-RJMCMC and LORETA method. Localization results are shown in Figure 5.11.

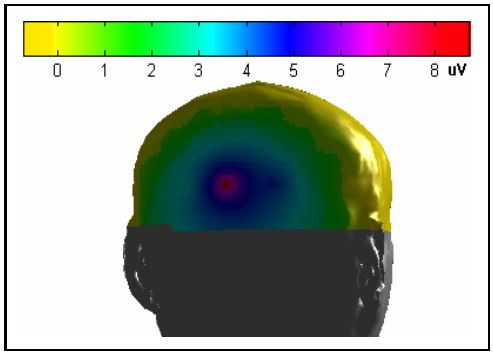

Figure 5.10 Scalp topography produced by the activation of ten dipole sources in primary visual cortex.

A threshold, 40 % of the maximum magnitude is applied on current density found by LORETA. Current distributions found by these two methods are both concentrated on primary visual cortex. Even though Bayesian MCMC source reconstruction can be classified as an ECD approach, comparing to an imaging approach, LORETA, it was equally effective to localize widespread neural activity.

5.5.2 Subcortical Neural Activity

To compare the performance of Bayesian PT-RJMCMC method with LORETA regarding the problem with *depth biasing*, an illustrative example of source configuration is used. EEG data is produced by the activation of two thalamic sources shown in Figure 5.12(a) .

LORETA was unable to recover deep sources in the thalamus (Figure 5.12(b)).

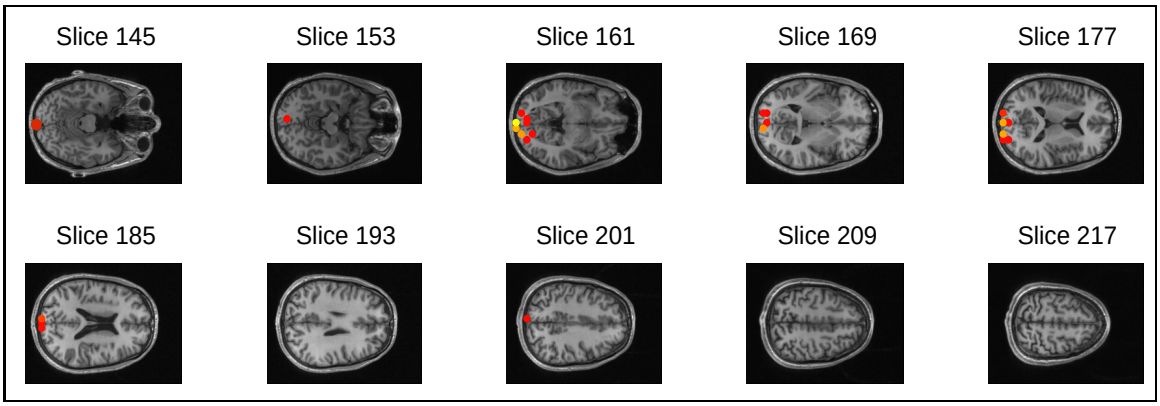

(a) Bayesian PT-RJMCMC results.

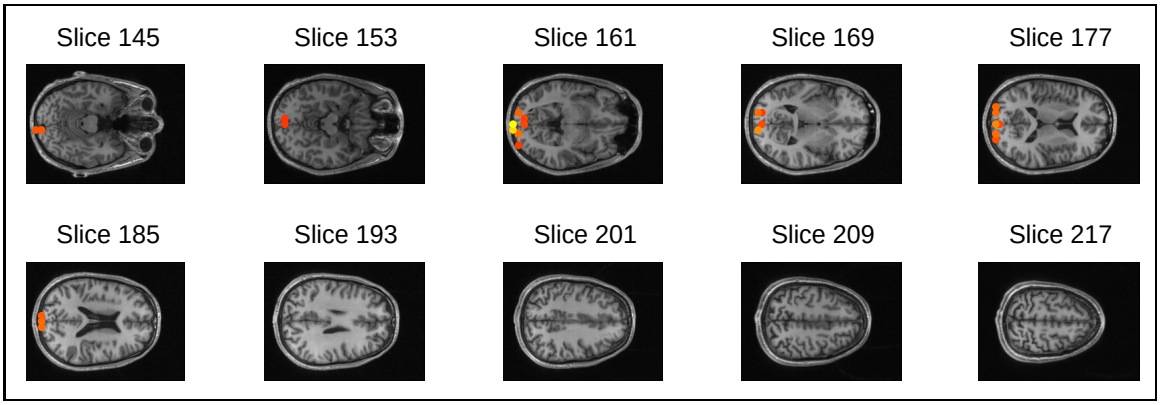

(b) LORETA results.

Figure 5.11 EEG produced by the activation of ten dipole sources in primary visual cortex are localized by (a) Bayesian PT-RJMCMC (b) LORETA method.

Again in this example as already shown in Simulation B, the MCMC approach gives accurate estimates (Figure 5.12(c)).

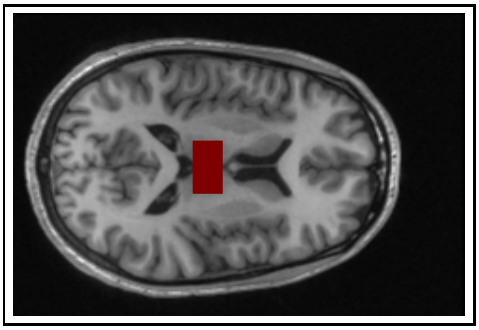

(a) Source Location.

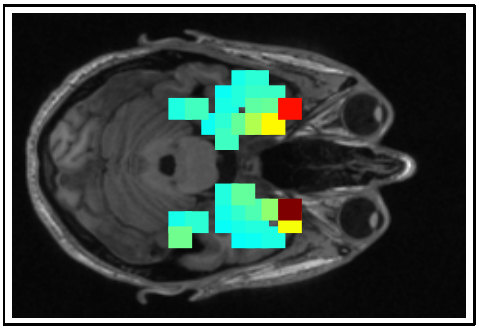

(b) LORETA result.

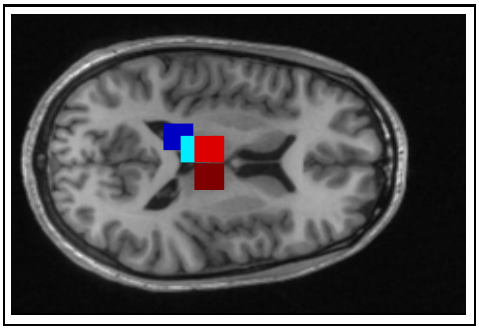

(c) MCMC result.

Figure 5.12 Simulated EEG data is generated by the activity of two dipoles, locating at thalamus. (a)Original source locations, (b)LORETA (c) MCMC source localization results.

6. APPLICATION TO EVENT RELATED POTENTIALS (ERPs)

To further investigate the feasibility of our proposed Bayesian MCMC source localization method, we tested it with ERP data, obtained from SPM web site [43]. This dataset contains EEG, fMRI and structural MRI data on the same subject within the same paradigm, which allows a basic comparison of faces versus scrambled faces. It has been used once by Henson *et al.* in [44] to study spatial and temporal aspects of face processing in the human brain. Although we used EEG data to localize N170 wave essentially by MCMC method, source localization is also done by LORETA and MUSIC methods and fMRI data are analyzed by SPM5 software to evaluate and compare different results.

6.1 Overview of Experiment

6.1.1 Paradigm

In this experiment, 86 faces and 86 scrambled faces are randomly presented to the subject whose task was to rate the left/right symmetry. Faces were presented for 600 ms, every 3600 ms. The subject was instructed not to blink while the fixation cross was present on the screen. The scrambled faces shown in Figure 6.1 were created by 2D Fourier transformation, random phase permutation, inverse transformation and outline-masking of each face. Half the faces were famous, but this factor is collapsed in our analysis. Two event types that were compared in this analysis are:

- event-type 1= familiar and unfamiliar faces (F)
- event-type 2= scrambled faces (S)

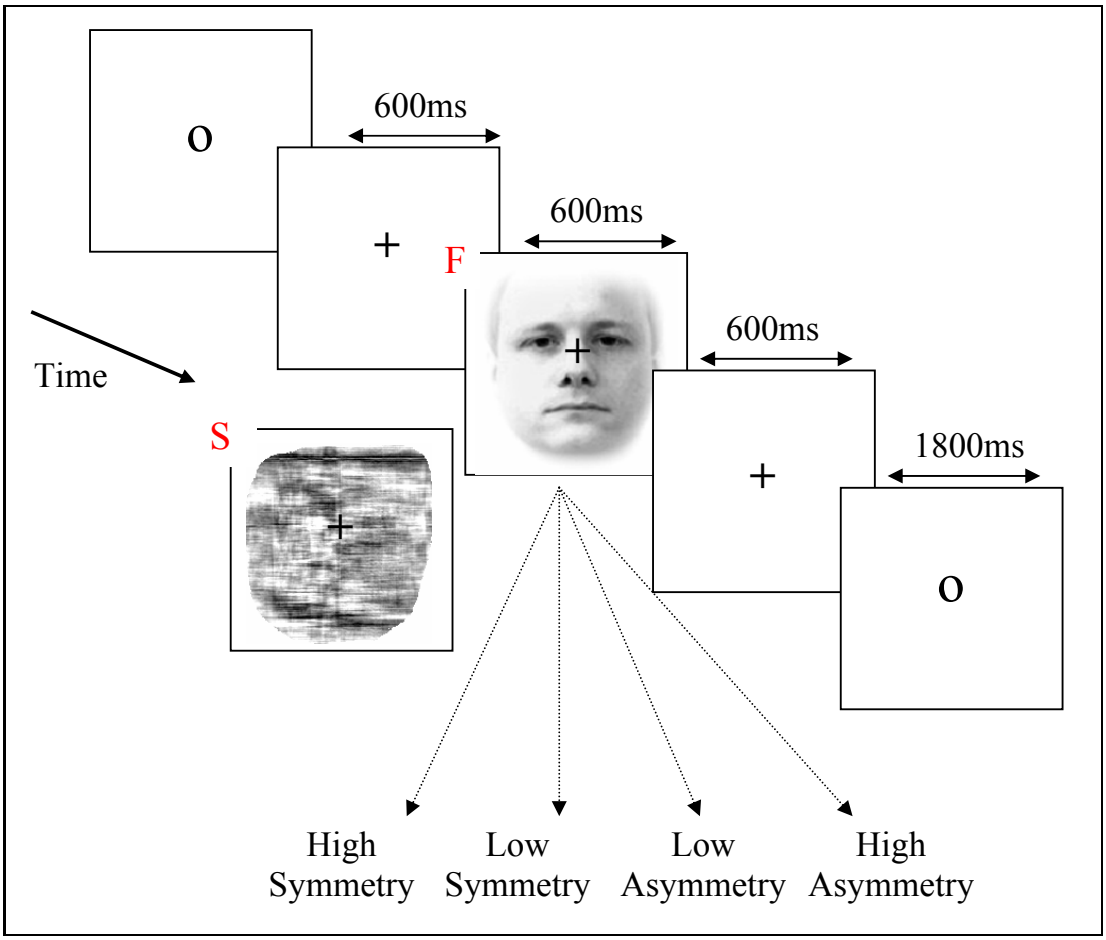

Figure 6.1 Face paradigm. One trial in the experimental paradigm involves either a Face (F) or Scrambled face (S).

6.1.2 ERP Component N170

Responses to faces and non-face stimuli are compared by Jeffreys in 1989 [45], and he found a difference between 150 and 200 ms at central midline sites that he named *vertex positive potential*. Jeffreys noted that this effect inverted in polarity at more lateral sites, but he did not have any recordings from electrode sites over inferotemporal cortex. More recent studies [46] have found that faces elicit a more negative potential than non face stimuli at lateral occipital electrode sites, especially over the right hemisphere, with a peak at approximately 170 ms. Although, the ERP component N170 is firstly defined as "the first posterior negative deflection following the visual presentation of a picture of a face, peaking at occipito-temporal sites at around 170 ms" [46], face specificity of N170 is a topic of considerable debate as some studies show that N170 can also occur for other highly familiar stimuli, such as words [47], [48].

A few studies have investigated neural sources underlying N170 with source localization methods. A recent study of Itier and Taylor used LAURA method with no *a priori* assumption on the number of the sources and their locations, and N170 sources have been localized to the superior temporal sulci [49]. Schweinberger *et al.* used Brain Electrical Source Analysis software based on minimum norm estimation and located N170 generators at the lateral occipitotemporal cortex [50]. Other studies based on ECD approach found entirely different generators such as fusiform gyri (FG) [51], or the FG and additional structures such as the lingual gyri [52]. The heterogeneity of results can be caused not only by the use of different paradigms and record techniques in experiments but also by the ill-posed nature of the EEG inverse problem: Different assumptions and source reconstruction methods lead to different solutions.

In Hansen's study, which we use the same data set, no N170 source reconstruction is done but differences between F and S in scalp topographies were tested by analysis of variances (ANOVAs) of amplitude differences and scalp potential and current source density (CSD) maps were created by spline interpolation [44]. Based on these results, Hansen *et al.* claimed that N170 is most likely generated in the superior

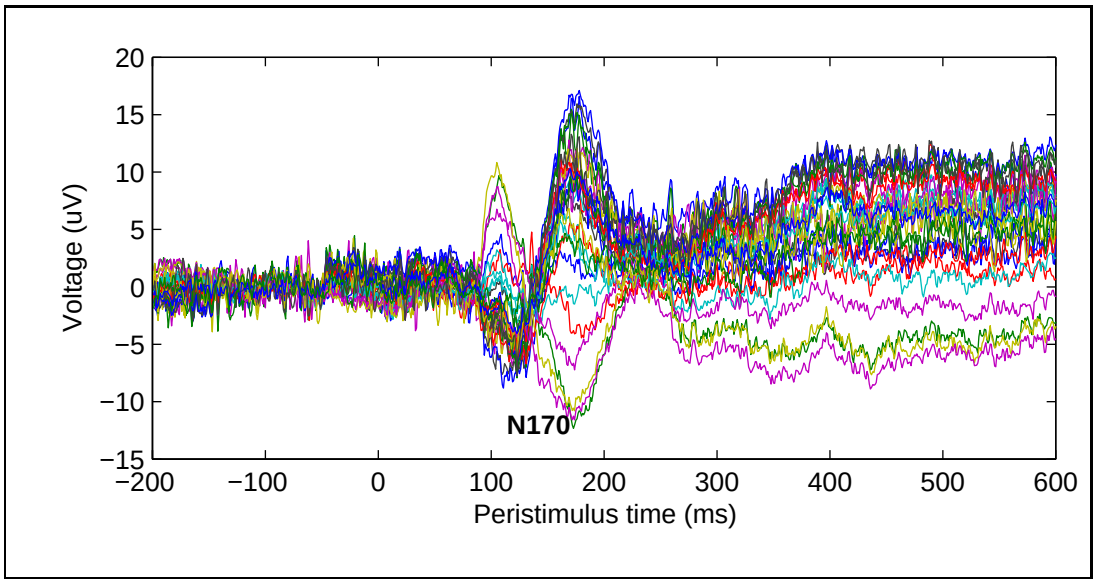

Figure 6.2 Event-Type I (F) spatiotemporal ERP data. 30 channels are overlapped.

temporal region and dipole source results would confirm the activated regions which were determined by SPM analysis of the fMRI data.

6.1.3 Multimodal Dataset

The EEG data were acquired on a 128-channel ActiveTwo system, sampled at 2048 Hz, plus electrodes on left earlobe, right earlobe, and two each to measure HEOG and VEOG. The original continuous data were converted from BDF format to SPMEEG format referencing to the average of the left and right earlobe electrodes (for consistency with [44]), and epoched from -200ms to +600ms. The epochs were then averaged according to the two trial types (F, S). As described in the previous chapter, our head model is designed for 30 channel electrodes; to reduce channel number and choose appropriate electrode locations we used SPM5 software. Noise covariance is estimated using prestimulus data. The resulting event-type I ERP data are visualized in Figure 6.2.

The fMRI data were acquired using a Trajectory-Based Reconstruction (TBR) gradient-echo EPI sequence on a 1.5T Sonata. There were 32, 3mm slices of $3 \times 3mm^2$

pixels, acquired in a sequential descending order with a TR of 2.88s. fMRI data are preprocessed with realignment, slice timing, spatial normalization, co-registration and smoothing steps of SPM5 software. These transformations aim to reduce unwanted variance components in the voxel time series that are induced by movement or shape differences among a series of scans.

6.2 Statistical Analysis of fMRI Data

After the preprocessing steps, fMRI images are ready to be analyzed. SPM makes the statistical analysis of fMRI data into two steps: fMRI model specification and estimation.

The general linear model embedded in the SPM software provides a framework for modeling of the data. The aim of the general linear model is to explain the variation of the time course $y_1 ... y_i ... y_n$, in terms of a linear combination of explanatory variables and an error term. The general linear model in matrix form can be written as

$$\vec{Y} = X\vec{\beta} + \vec{\epsilon} \tag{6.1}$$

where $\vec{Y}$ is the vector of observed pixel values, $\vec{\beta}$ is the vector of parameters and $\vec{\epsilon}$ is the vector of error terms. The matrix X is known as design matrix. Its number of rows is equal to the number of scans in the experiment and its column number is equal to the number of explanatory variables.

In our case we have two conditions, F and S, which constitute the first two columns of the design matrix, and six regressor parameters derived by the realignment step of preprocessing. These parameters are used to cancel some of the residual movement-related effects. The final column is the baseline of brain activity. We derived the design matrix by a first level analysis, using 215 preprocessed images. Canonical Hemodynamic Response Function (HRF)without time derivatives was chosen to model the hemodynamic response. The design matrix is visualized in Figure 6.3.

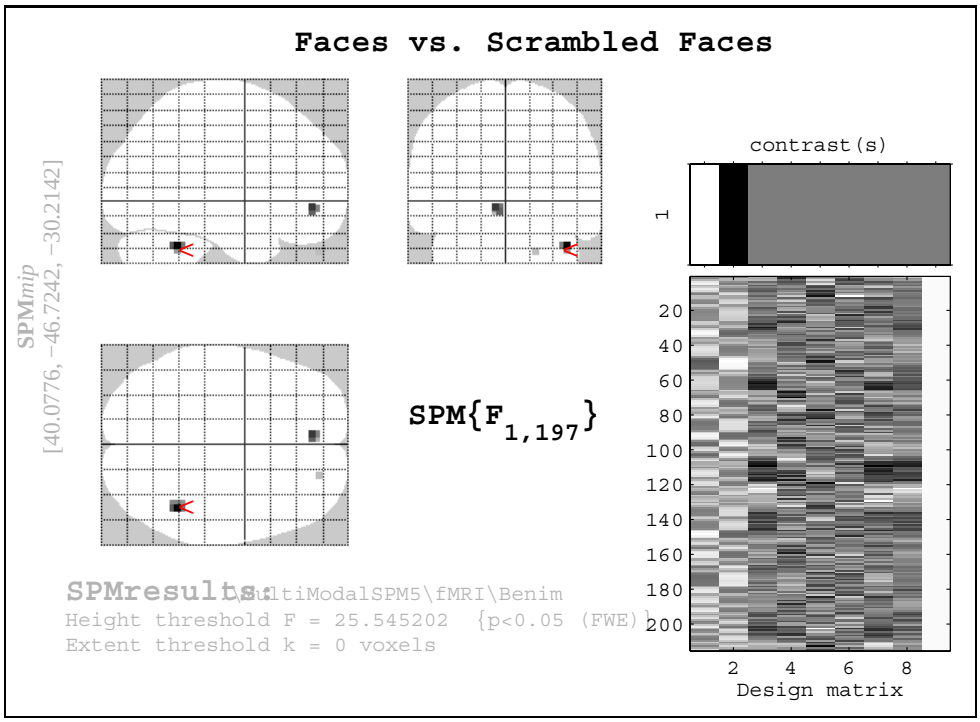

Figure 6.3 SPM$\{F\}$ for faces versus scrambled faces.

In the fMRI model estimation step, model parameters are estimated using Restricted Maximum Likelihood (ReML) estimation. GLM characterizes relationships between the experimental manipulations and the observed data - multiple effects all within the same design matrix. So to focus on a particular characteristic, condition, or regressor we use contrasts. t-tests tell us whether there is a significant increase or decrease in the contrast specified; F-tests tell us whether there is a significant difference between the conditions in the contrast [53]. To see the regions that respond differentially between faces and scrambled faces, an F-contrast ($[1 \ -1]$) was defined. This contrast identified regions in which the parameter estimate for the canonical HRF differs reliably between faces and scrambled faces. This could include regions that show both a greater relative response for faces, and regions that show a greater relative response for scrambled faces. If the resulting SPM$\{F\}$ is thresholded at $p < .05$ family-wise error (FWE) corrected, the resulting maximum intensity projection (MIP) should be like that in Figure 6.3.

Only two regions survive correction: right fusiform and orbitofrontal cortex (Figure 6.4). They are a subset of the regions identified by the same contrast in a

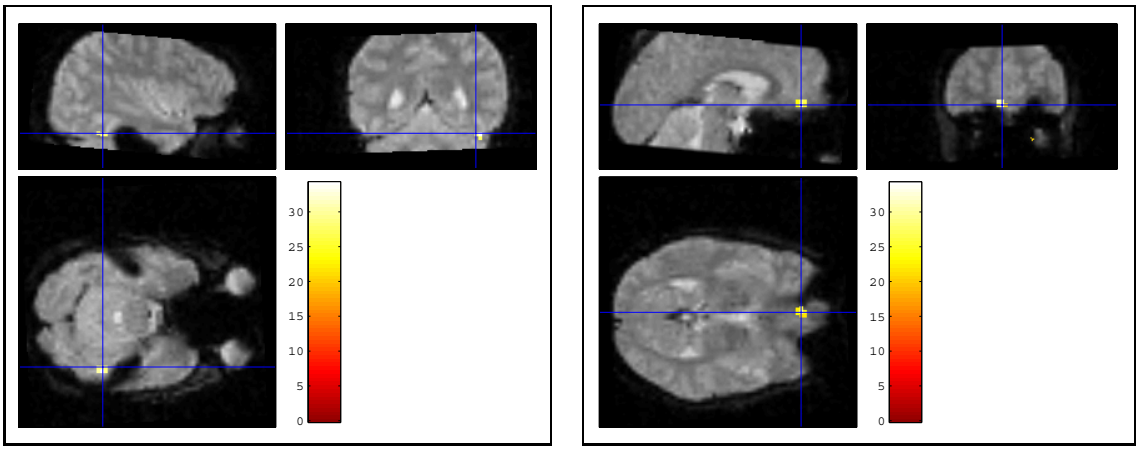

(a) Right fusiform

(b) Orbitofrontal cortex.

Figure 6.4 fMRI activation map. Two regions (a) right fusiform, (b) orbitofrontal cortex respond differently to faces and scrambled faces.

group of 18 subjects in [44]. At a lower threshold (e.g, $p<.01$), additional activation can be seen in left fusiform, as well as other regions.

6.3 ERP Source Reconstruction

For the EEG data, the difference between faces and scrambled faces is maximal around 170ms, appearing as an enhancement of a negative component (N170) at occipito-temporal channels, or enhancement of a positive peak (vertex positive potential) at Cz. These effects are shown as time series in Figure 6.5 and as a differential scalp topography in Figure 6.6 .

To realize instantaneous source reconstruction process, F and S potentials recorded with 30 channels at 170ms, are extracted from the whole spatiotemporal data.

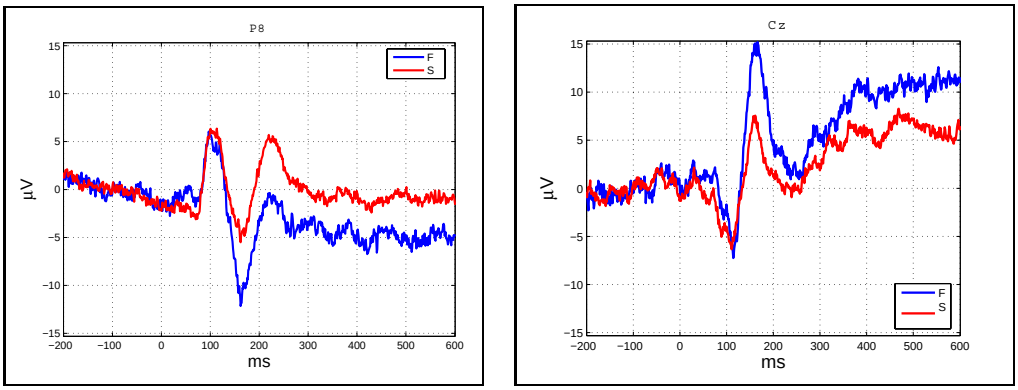

(a) EEG time series recorded at P8. (b) EEG time series recorded at Cz.

Figure 6.5 Sensor time courses for face data at occipito-temporal electrode P8 (a) and vertex Cz (b) for faces (blue) and scrambled faces (red).

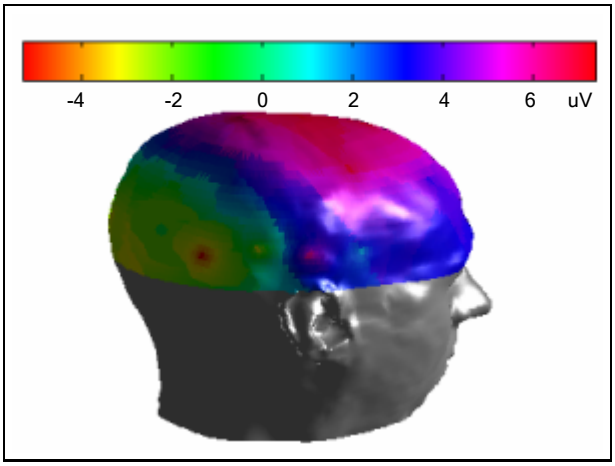

Figure 6.6 Differential EEG scalp topography for faces minus scrambled faces at t = 170ms post-stimulus.

6.3.1 MCMC method results

Source reconstruction is done separately for F and S potentials namely, we first localized faces potentials, then scrambled faces potentials and like in SPM approach we applied a contrast between two source localization results:

$$\vec{J}_{F-S} = |\vec{J}_F - \vec{J}_S| \tag{6.2}$$

$\vec{J}_F$ represents dipole currents distribution that generates F potentials, $\vec{J}_S$ represents dipole currents distribution that generates S potentials and $\vec{J}_{F-S}$ vector will show dipole sources that have a greater magnitude for faces of scrambled faces stimulus.

Our hybrid PT-RJMCMC algorithm were run with five chains, for 30000 iterations. For each data, we conducted five runs to check the consistency of results. To monitor the convergence, we used the PSRF test and $\hat{R}$ values for each dipole parameters were less than 1.1. First 25% of iterations were discarded for each chain as the burn-in period. Prior distributions for dipole parameter set x were:

- N: Uniform between $N_{min} = 1$ and $N_{max} = 5$,
- $\vec{r}$: Uniform over 1360 predefined voxels,
- $\vec{m}$: Uniform between $m_{min} = -100nAm$ and $m_{max} = 100nAm$, with a step size of 0.01nAm.

Sampled a posteriori dipole parameter distributions $p(x_F|\vec{V_F})$ and $p(x_S|\vec{V_S})$ are used to generate current distribution vectors $\vec{J}_F$ and $\vec{J}_S$, and the above defined contrast is applied. The resulting $\vec{J}_{F-S}$ is shown in Figure 6.7 . This differential current magnitude distribution is concentrated at two clusters: (i)superior parietal lobule, (ii)right middle-superior temporal gyrus. The absolute value of the reconstructed activity was thresholded at 50 % of its maximum, leaving the set of suprathreshold clusters of active sources. Activation at these clusters, including right fusiform gyrus is seen at the current density maps in Figure 6.8. The images show differences in absolute current

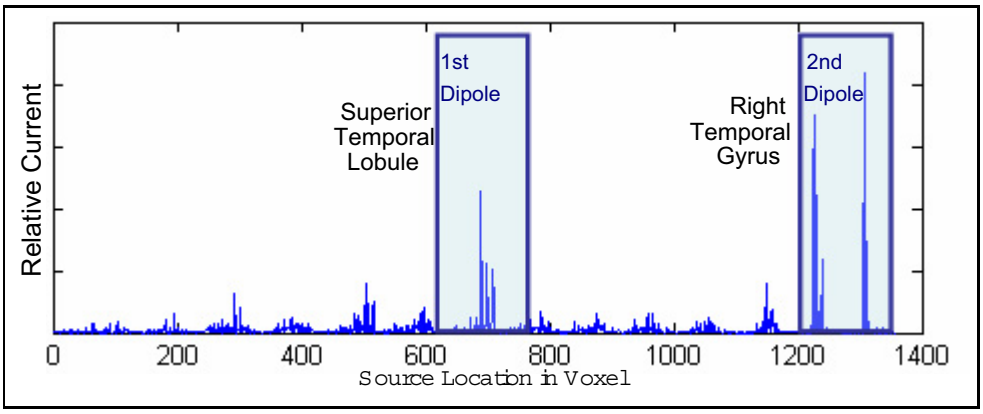

Figure 6.7 Differential dipole current magnitude distribution $\vec{J}_{F-S}$ for faces minus scrambled faces at t = 170ms poststimulus found by MCMC.

at each voxel. The maximum difference is plotted in yellow and 25 % of the maximum difference in red.

We also localized directly the potential difference at 170ms between F and S, $\vec{V}_{F-S}$, and found exactly same clusters with the previous contrast study, $|\vec{J}_F - \vec{J}_S|$. This equality can not be mathematically proved as the current inverse operation is not linear. As shown in Eq. 3.5, to calculate the likelihood function, $p(\vec{V}|N, \vec{r}, \vec{m})$, at each iteration we are not using the complete lead field matrix K like in linear inverse methods, but only those columns respective to current location parameters. With this direct localization approach, active dipole number histogram shows that J_{F-S} current distribution vector can be confidently modeled with two dipoles (Figure 6.9). The first of the voxel pair with MAP probability locates at superior parietal and the second at right occipito-temporal region.

6.3.2 LORETA and MUSIC Inverse Solution

LORETA method's validity in ERP-type source reconstruction has been demonstrated in several studies of independent research groups [32]. Hence, LORETA is widely accepted as a reliable inverse method in ERP source localization and its results can be used to qualify the effectiveness of MCMC method in this N170 study.

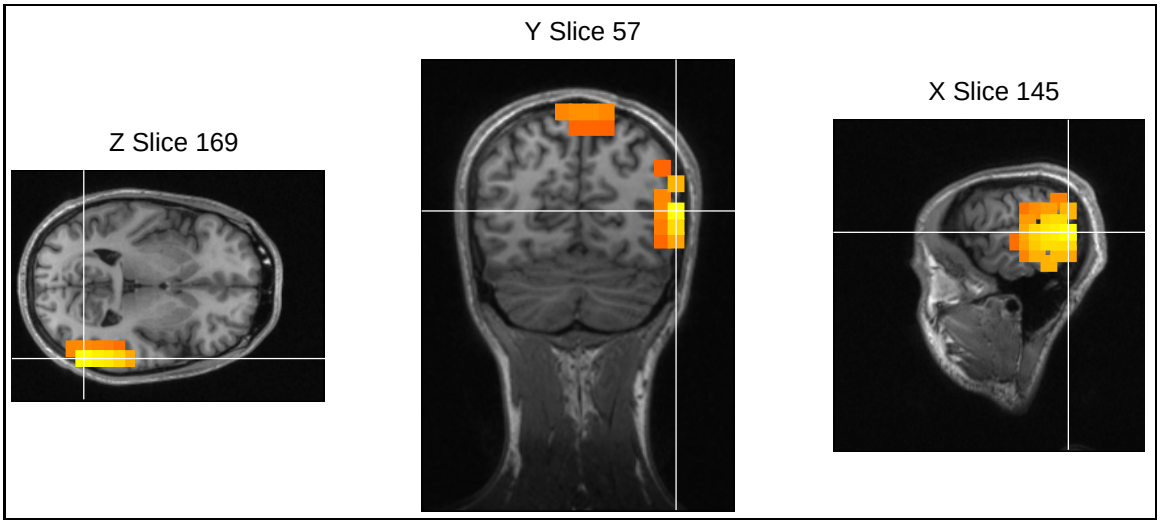

(a) The maximum difference is located at the right occipito-temporal region.

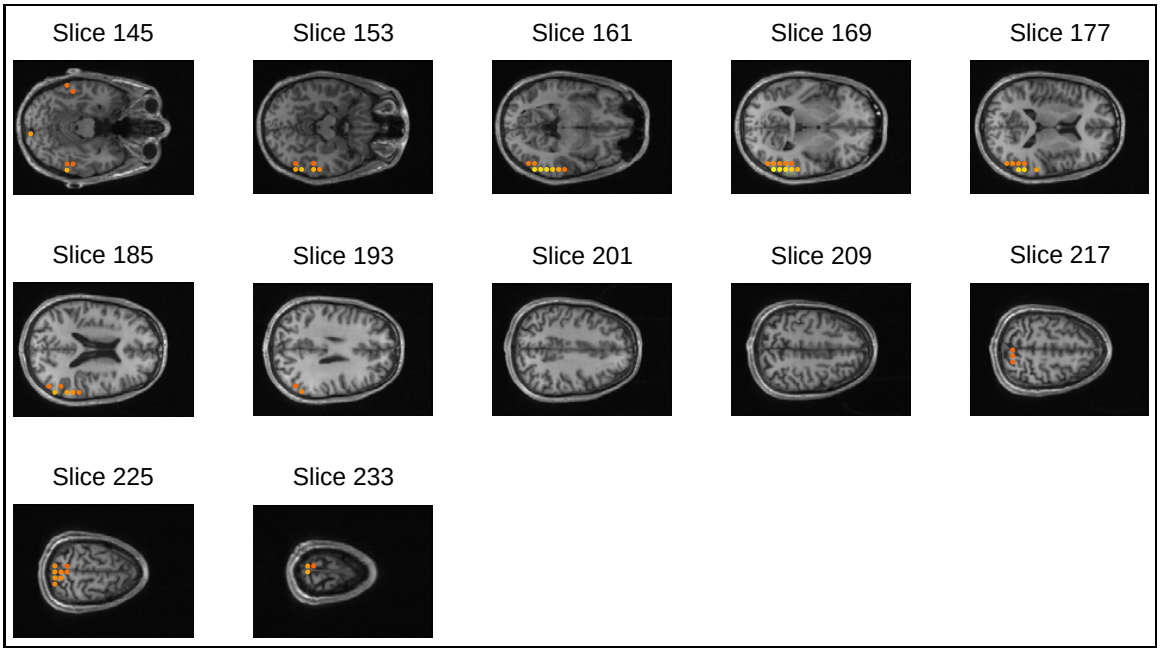

(b) Slice view of current density map.

Figure 6.8 Current density maps derived from the source reconstruction of ERPs in response to faces and scrambled faces, with PT-RJMCMC method. The plots show absolute differences between faces and scrambled faces at t=170ms post-stimulus.

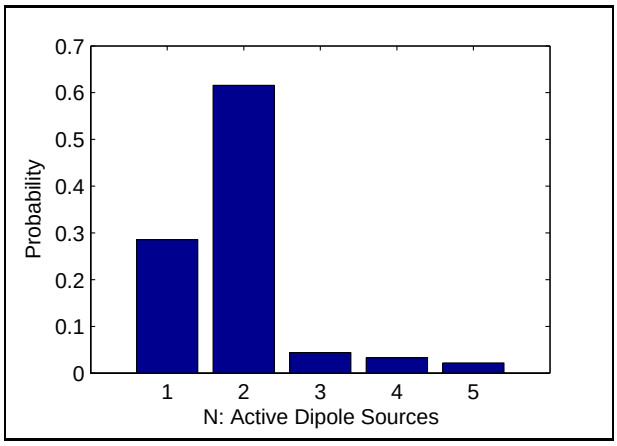

Figure 6.9 Probability of the number of dipoles, estimated from all PT-RJMCMC runs by counting the number of iterations of the Markov chains that contained one, two, three, four or five dipoles. A 60 % probability is found for the two dipoles.

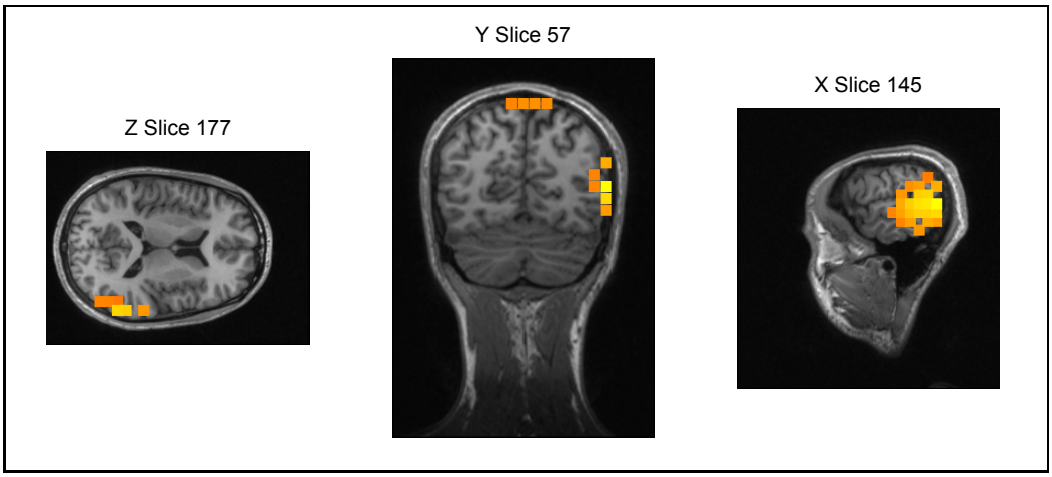

Figure 6.10 F and S potentials are localized with LORETA method. This figure represents the differential source localization result, $\vec{J}_F - \vec{J}_S$.

Figure 6.10 shows current density values of the voxels forming the LORETA inverse solution space. The maximum is found at superior temporal gyrus. Comparing with MCMC results, the density is concentrated at the same two clusters and the distance between two maxima is only 8mm: MCMC source reconstruction result are consistent with LORETA's solution.

Source analysis of MUSIC algorithm has found one active dipole, for this instantaneous ERP data, locating at the lingual gyrus. As shown in Figure 6.9 a 30 % probability was found for the one dipole by MCMC. Figure 6.11 shows that MUSIC

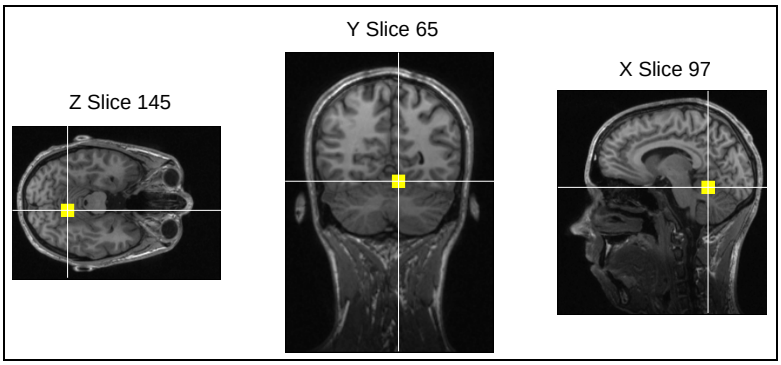

(a) MCMC result for N=1 active dipole.

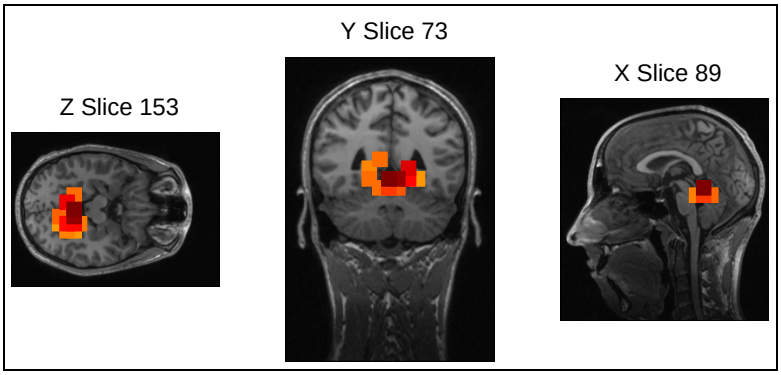

(b) MUSIC result.

Figure 6.11 Source localization of F-S by MCMC for one dipole (a) and MUSIC. Both points the same region: lingual gyrus.

result and MCMC result for one dipole, point the same region and the distance between two maxima is one voxel size. This result is not surprising as dipole source localization analysis in previous studies of Mnatsakanian *et al.* and Shibata *et al.* indicated that generators for the N170 elicited by faces were located at the lingual gyrus at the late phase of the N170 [52], [54].

7. DISCUSSION AND CONCLUSIONS

This study demonstrates the use of a Bayesian method for analyzing EEG data that directly addresses the ill-posed character of the inverse problem by allowing probabilistic inferences to be drawn about dipole parameters from a large number of possible that both fit the data and prior assumptions.

The approach presented here differs from previous studies [11], [10] in which restrictive assumptions about the neural activity are introduced as the prior information and posterior distributions are explored by point estimations. Contrary to conventional Bayesian inverse methods that give only a single best solution, sampling posterior dipole parameter distributions with MCMC methods provides multiple source reconstruction results. The multiplicity of the solutions is not a drawback of the method, but a direct consequence of the ill-posed EEG inverse problem. All solutions obtained by MCMC were plausible solutions and finding only one of them only partially solves the problem.

The power of MCMC methods lies principally in its simplicity and wide applicability of the basic algorithm. However, the original Metropolis-Hastings algorithm was not adequate for the current inverse model as the dimension of the parameters were assumed to be unknown. In the literature, MCMC algorithms were applied to MEG inverse problem on spherical head models. To our knowledge, there is no study that indicates which specific MCMC algorithm and tuning parameters should be chosen to solve EEG inverse problem, among the dozen or more that exist.

Gibbs sampler requires full conditional distributions for all dipole parameters. Moreover when the dimension of the solution space is not fixed at each iteration, to sample some dipole parameters conditional on the remainder hardly makes sense. Therefore, Hastings class of MCMC algorithms was adapted to the source reconstruction problem.

An RJMCMC algorithm coupled with parallel tempering that uses the Metropolis-Hastings kernel for computing the acceptance probability of a new dipole configuration is utilized as the underlying sampling technique. The sampler uses reversible moves, such as birth and death, and a symmetrical perturbation for sampling a candidate state given the current state, such that a jump between spaces of different dimensions is made possible. Since the major drawback of MCMC methods is their difficulty in escaping from local optima, heuristics such as simulated annealing and parallel tempering are used to make the sampling of the posterior distributions easier. We should note that the local optima problem in source reconstruction is not specific to MCMC samplers and other dipole analysis methods have also encountered this problem [55]. The convergence of the algorithm was diagnosed with PSRF, a test based on the analysis of variance. Experimental results demonstrating the effectiveness of the proposed algorithm has been provided for several EEG data sets.

Current density maps obtained from MCMC results and projected to the 3D brain volume or cortical surface, provide a link between ECD and imaging approaches. During MCMC iterations dipole topography were fitted to the data with an ECD approach as the upper limit for the number of the active dipole ($N_{max} = 5$) was much less than the number of predefined set of dipoles ($N_v = 1360$). Location probability weighted MAP magnitude projection offers not only a distributed solution which covers the whole brain volume but also a double check for the consistency of the results comparing to location-only or magnitude-only mapping.

Experiment on both simulated and empirical data have shown the value and the capability of Bayesian MCMC method. Experiments with simulated data show that MCMC method can accurately localize widespread EEG generators whereas well-known deterministic ECD approach MUSIC is only reliable for focal activity. Furthermore, MCMC approach does not have depth biasing which is an intrinsic problem for LORETA.

In the ERP source localization study, we investigated what neural regions shows differential activation patterns when the subject is shown faces compared to scrambled

faces. Numerous imaging studies have confirmed engagement of the fusiform gyrus during a range of face perception tasks. Bayesian MCMC inverse results are consistent with fMRI, and LORETA and MUSIC source localization analysis of faces minus scrambled faces in that face processing is lateralized to the right hemisphere and in particular to fusiform gyrus.

It should be noted that in our study, the PT-RJMCMC or SA-RJMCMC algorithm failed to give all the different solutions for a given EEG data and "zero localization error" for all type of dipole configurations. Methodological research is still needed to improve reconstruction results. "Zero localization error" may be achieved by introducing physiological, functional priors and spatially informed basis functions into the Bayesian formulation preferably without restricting the solution space.

Our results show that adequately chosen MCMC algorithms are able to solve the instantaneous EEG inverse problem even under difficult conditions like an unknown number of sources, or a high noise level. However, a number of issues have still to be solved for practical application of MCMC methods. The most important one is undoubtedly their extension to spatiotemporal analysis, a point that is already covered by Schmidt *et al.* in MEG inverse problem [12]. Prospective studies about MCMC methods can cover full spatiotemporal analysis and information acquired from other neuroimaging modalities especially from fMRI can be introduced in the Bayesian model.

APPENDIX A. FORWARD MODEL

In this study, the forward problem is solved by the Boundary Element Method (BEM) which is a numerical approximation technique which partitions the surface of a volume conductor into closed triangular meshes. This technique has been used in dipole source localization of brain electromagnetic activity since the end of 80's. The human head is modeled as three homogeneous conductor layers; the outermost surface being the boundary for the scalp, and the intermediate and the innermost being the one for the skull and the brain, respectively.

In order to apply the BEM, a realistic head model has to be formed and its surfaces must be tesselated into triangles. The electrical potential *v(s)* at any surface point s can be represented by an integral equation:

$$\frac{\sigma_i^+ + \sigma_i^-}{2} v(s) = \vec{V}_\infty - \frac{1}{4\pi} \sum_{j=1}^{3} \frac{\sigma_j^+ + \sigma_j^-}{2} \oint_{Sj} dS' n(r') . \frac{|s - r'|}{|s - r'|^3} v(s) \tag{A.1}$$

n is the unit normal vector to the surface and $\vec{V}_\infty$ is the potential in an infinite extent conductor with unit conductivity due to a primary source at r' with strength p:

$$\vec{V}_\infty = \frac{1}{4\pi} \frac{p(s - r')}{|s - r'|^3} \tag{A.2}$$

The conductivities outside and inside the surface S_j are σ_j^+ and σ_j^- respectively.

The conductor surfaces S_j are approximated by small triangles. Surfaces of the brain, skull and scalp are tesselated with 2000, 1200 and 1200 triangles respectively. These tesselated surfaces are shown in Figure A.1.

For the BEM, the center of gravity method is used which is based on the assumption that the potential at the center of gravity is the same as the potential at everywhere on the triangle. The surface integral in Eq. A.1 reduces to a sum and is evaluated over each triangle as a secondary source contribution to the potential. There

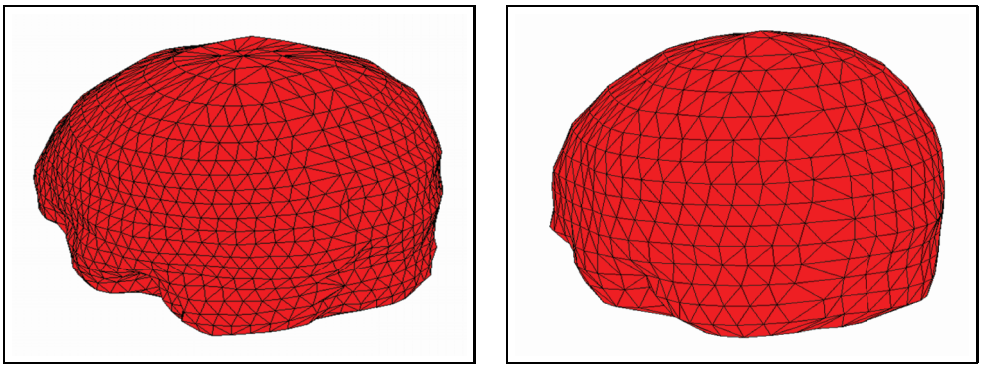

(a) Brain. (b) Skull.

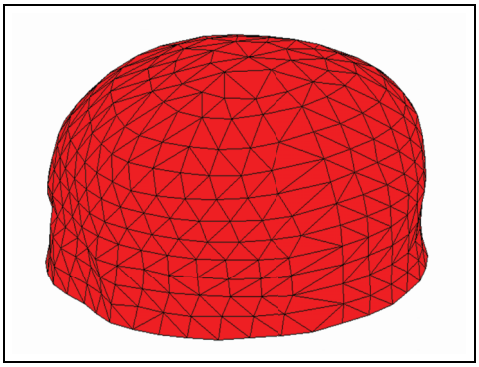

(c) Scalp.

Figure A.1 Tesellated a) brain, b) skull and c) scalp surfaces.

are several methods for approximating the potential on the triangles like constant, linear or quadratic polynomial interpolation. By these approximations, Eq. A.1 becomes a linear system of equations to be solved for the potentials on the triangles.

APPENDIX B. CODE DESCRIPTIONS

In this appendix, the names of the files found in Appendix C (CD-ROM) are outlined.

B.1 MCMC Samplers

B.1.1 PTRJMCMC.m

Performs Bayesian PT-RJMCMC algorithm for the inverse solution of the dipole parameters.

Inputs: **K**, $n_e \times n_v \times 3$ lead field matrix, **V** measured instantaneous EEG potentials, **itnum**, iteration number, **teknum** number of runs, **NewVolumeGray**, matrix containing gray matter coordinates of the head model, **P** matrix containing transitions probabilities between model parameters **R** head model spatial resolution.

Outputs: **p** log-probability for at each iteration, **S** matrix containing the history of the Markov Chains, **J1**, location probability weigthed current density map, **DN**, posterior probability distribution for dipole number, **L**, posterior probability distribution for dipole location, **M**, posterior probability distribution for dipole magnitudes.

Called by: Command line.

B.1.2 SARJMCMC.m

Performs Bayesian SA-RJMCMC algorithm for the inverse solution of the dipole parameters.

Inputs: **K**, $n_e \times n_v \times 3$ lead field matrix, **V** measured instantaneous EEG potentials, **itnum**, iteration number, **teknum** number of runs, **NewVolumeGray**, matrix containing gray matter coordinates of the head model, **P** matrix containing transitions probabilities between model parameters **R** head model spatial resolution, **T**, maximum temperature.

Outputs: **p** log-probability for at each iteration, **S** matrix containing the history of the Markov Chains, **J1**, location probability weigthed current density map, **DN**, probability distribution for dipole number, **L**, posterior probability distribution for dipole location, **M** posterior probability distribution for dipole magnitudes.

Called by: Command line.

B.1.3 IS.m

Performs Bayesian IS algorithm for the inverse solution of the dipole parameters.

Inputs: **K**, $n_e \times n_v \times 3$ lead field matrix, **V** measured instantaneous EEG potentials, **itnum**, iteration number, **teknum** number of runs.

Outputs: **p** log-probability for at each iteration, **S** matrix containing the history of the Markov Chains, **J1**, location probability weigthed current density map, **DN**, probability distribution for dipole number, **L**, posterior probability distribution for dipole location, **M** posterior probability distribution for dipole magnitudes.

Called by: Command line.

B.2 CONVERGENCE MONITORING

B.2.1 psrf.m

Implements psrf convergence test.

Inputs: $\mathbf{X}$, is a $N \times D \times M$ matrix which contains M MCMC simulations of length N, each with dimension D.

Outputs: $\mathbf{R}$, PSRF ($R = \frac{V}{W}^{\frac{1}{2}}$) in row vector of length D, **neff**, estimated effective number of samples $\frac{M \times N \times V}{B}$, $\mathbf{V}$, estimated mixture-of-sequences variances, $\mathbf{W}$, estimated within sequence variances, $\mathbf{B}$, estimated between sequence variances.

Called by: Command line.

APPENDIX C. CD-ROM

The scripts mentioned in Appendix B are found in CD-ROM which is enclosed inside the back cover. Minimum system requirements: Matlab V6 (Release 12), a pentium based PC with at least 128 MB RAM.

REFERENCES

1. Nunez, P. L., *Electric Fields of the Brain: The neurophysics of EEG*, New York: Oxford University Press, 2005.

2. Baillet, S., J. C. Mosher, and R. M. Leahy, "Electromagnetic brain mapping," *IEEE Signal Processing Magazine*, Vol. 18, pp. 14–30, November 2001.

3. Michel, C., M. Murray, G. Lantz, S. Gonzale, L. Spinelli, and R. G. de Peralta, "EEG source imaging," *Clinical Neurophysiology*, Vol. 115, no. 10, pp. 2195–2222, 2004.

4. Sarvas, S., "Basic mathematical and electromagnetic concepts of the biomagnetic inverse problem," *Phys. Med. Biol.*, Vol. 32, pp. 11–22, November 1987.

5. Koles, Z. J., "Trends in EEG source localization," *Electroencephalogr. Clin. Neurophysiol.*, Vol. 106, no. 2, pp. 127–37, 1998.

6. Duru, A. D., "Source localization of electrical dipoles in electroencephalogram (EEG)," Master's thesis, Bogazici University, Istanbul, Turkey, 2004.

7. Ademoglu, A., A. D. Duru, and T. Demiralp, "Source localization of topographic EEG maps prefiltered by spatiotemporal wavelets," *IX. International Conference on Cognitive Neuroscience*, 2005.

8. Emir, U. E., A. D. Duru, A. Ademoglu, and A. Akin, "Coregistration of fNIRS data on to the realistic head model.," *Conf. Proc. IEEE Eng. Med. Biol. Soc.*, Vol. 3, pp. 3184–7, 2005.

9. Duru, A. D., A. Bayram, T. Demiralp, and A. Ademoglu, "Source localization of subtopographic brain maps for event related potentials (ERP)," *Proceedings of the 28th IEEE EMBS Annual International Conference, New York*, pp. 4832 – 4834, Aug. 2006.

10. Baillet, S., and L. Garnero, "A Bayesian approach to introducing anatomo-functional priors in the EEG/MEG inverse problem," *IEEE Trans. Biomed. Eng.*, Vol. 44, no. 5, pp. 374–385, 1997.

11. Leahy, J. W. P. R. M., and J. C. Mosher, "MEGbased imaging of focal neuronal currrent sources," *IEEE Trans. Medical Imaging*, Vol. 16, no. 3, pp. 338–348, 1997.

12. Schmidt, D. M., J. S. George, and C. C. Wood, "Bayesian inference applied to the electromagnetic inverse problem," *Hum. Brain Mapp.*, Vol. 7, pp. 195–212, 1999.

13. Liu, A. K., A. M. Dale, and J. W. Belliveau, "Monte Carlo simulation studies of EEG and MEG localization accuracy," *Hum. Brain Mapp.*, Vol. 16, pp. 47–62, 2002.

14. Baillet, S., *Toward Functional Brain Imaging of Cortical Electrophysiology. Markovian Models for Magneto and Electroencephalogram Source Estimation and Experimental Assessments.* PhD thesis, University of Paris XI, Paris, France, 1998.

15. Nunez, P. L., and R. B. Silberstein, "On the relationship of synaptic activity to macroscopic measurements: Does co-registration of EEG with fMRI make sense?," *Brain Topography*, Vol. 13, no. 2, pp. 79–97, 2000.

16. Kandel, E. R., and J. H. Schwartz, *Principles of Neural Science*, New York: Elsevier, 1985.

17. Nunez, P. L., *Neocortical dynamics and human EEG rhythms*, New York: Oxford University Press, 1995.

18. Mitzdorf, U., "Properties of the evoked potential generators: Current source-density analysis of visually evoked potentials in the cat cortex.," *International Journal of Neuroscience*, Vol. 33, pp. 33–59, 1987.

19. Dagnelie, G., H. Spekreijse, and B. van Dijk, "Topography and homogeneity of monkey V1 studied through subdurally recorded pattern-evoked potentials," *Visual Neuroscience*, Vol. 3, pp. 509–25, 1989.

20. Barth, D. S., and S. Di, "Three-dimensional analysis of auditory-evoked potentials in rat neocortex," *Journal of Neurophysiology*, Vol. 64, pp. 1527–36, 1990.

21. Hämäläinen, M., R. Hari, R. Ilmoniemi, J. Knuutila, and O. Lounasmaa, "Magnetoencephalography: Theory, instrumentation and applications to the noninvasive study of human brain function," *Rev. Mod. Phys.*, Vol. 65, no. 2, pp. 413–497, 1993.

22. Tesche, C. D., and J. Karhu, "Theta oscillations index human hippocampal activation during a working memory task," *Proc. Natl. Acad. Sci. USA*, Vol. 97, pp. 919–924, 2000.

23. Tesche, C. D., J. Karhu, and S. Tissari, "Non-invasive detection of neural population activity in human hippocampus," *Cognitive Brain Research*, Vol. 4, pp. 39–47, 1996.

24. Tesche, C. D., and J. Karhu, "Somatosensory evoked magnetic fields arising from sources in the human cerebellum," *Brain Res.*, Vol. 774, pp. 21–31, 1997.

25. Tenke, C. E., C. E. Schroeder, J. C. Arezzo, and H. G. Vaughan., "Interpretation of high-resolution current source density profiles: A simulation of sublaminar contributions to the visual evoked potential," *Exp. Brain Res.*, Vol. 94, pp. 183–192, 1993.

26. Parkkonen, L., and J. Mäkelä, "MEG sees deep sources: Measuring and modelling brainstem auditory evoked fields," in *Proceedings of the 13th International Conference on Biomagnetism*, pp. 107–109, Berlin, Germany: VDE Verlang, 2002.

27. Moses, S. N., J. M. Houck, T. Martin, F. M. Hanlon, J. D. Ryan, R. J. Thoma, M. P. Weisend, E. M. Jackson, E. Pekkonen, and C. D. Tesche, "Dynamic neural activity recorded from human amygdala during fear conditioning using magnetoencephalography," *Brain Research Bulletin*, Vol. 71, pp. 451–460, 2007.

28. Sato, M., T. Yokhioka, S. Kajihara, K. Toyama, N. Goda, K. Doya, and M. Kawato, "Hierarchical bayesian estimation for MEG inverse problem," *Neuroimage*, Vol. 23, pp. 806–826, 2004.

29. Phillips, C., J. Mattout, M. D, P. Maquet, and K. J. Friston, "An empirical Bayesian solution to the source reconstruction problem in EEG," *Neuroimage*, Vol. 24, no. 4, pp. 997–1011, 2005.

30. Mosher, J. C., and R. M. Leahy, "Recursive MUSIC: A framework for EEG and MEG source localization," *IEEE Trans. Biomed. Eng.*, Vol. 45, pp. 1342–45, 1998.

31. Ademoglu, A., T. Demiralp, Y. Istefanopulos, S. Comu, and B. Baykan, "Epileptic source localization using wavelet prefiltering and MUSIC scanning," in *Proceedings of the 25th Annual Int. Conference of the IEEE EMBS*, pp. 2366–69, Mexico: IEEE, 2003.

32. Pascual-Marqui, R. D., M. Esslen, K. Kochi, and D. Lehmann, "Functional imaging with low resolution brain electromagnetic tomography (LORETA): a review," *Methods & Findings in Experimental & Clinical Pharmacology*, Vol. 24, pp. 91–94, 2002.

33. Galka, A., O. Yamashita, T. Ozaki, R. Biscay, and P. Valdes-Sosa, "A solution to the dynamical inverse problem of EEG generation using spatiotemporal Kalman filtering," *NeuroImage*, Vol. 23, pp. 435–53, 2004.

34. Gelman, A., J. B. Carlinand, H. S. Stern, and D. B. Rubin, *Bayesian Data Analysis*, Boca Raton: CRC, 2003.

35. Hastings, W. K., "Monte Carlo sampling methods using Markov chains and their applications," *Biometrika*, Vol. 57, pp. 97–109, 1970.

36. Metropolis, N., A. W. Rosenbluth, M. N. Rosenbluth, A. H. Teller, and E. Teller, "Equations of state calculations by fast computing machine," *J. Chem. Phys.*, Vol. 21, pp. 1087–1091, 1953.

37. Green, P., "Reversible Jump Markov Chain Monte Carlo computation and Bayesian model determination," *Biometrika*, Vol. 82, no. 4, pp. 711–732, 1995.

38. Kirkpatrick, S., C. D. Gelatt, and M. P. Vecchi, "Optimization by simulated annealing," *Science*, Vol. 220, no. 4598, pp. 671–680, 1983.

39. De Weck, O., "Simulated Annealing," Multidisiplinary System Design Optimization, Lecture Notes, Massachusetts Institute of Technology, http://ocw.mit.edu/OcwWeb/Aeronautics-and-Astronotics, 2004.

40. http://www.fil.ion.ucl.ac.uk/spm.

41. Kaipio, J., and E. Somersalo, "Statistical inverse problems: Discretization, model reduction and inverse crimes," *Journal of Applied Computational Inverse Problems*, Vol. 198, pp. 493–504, 2007.

42. Trujillo-Barreto, N. J., E. Aubert-Vazquez, and P. A. Valdes-Sosa, "Bayesian model averaging in EEG/MEG imaging," *NeuroImage*, Vol. 21, pp. 1300–1319, 2004.

43. http://www.fil.ion.ucl.ac.uk/spm/data/mmfaces.html.

44. Henson, R. N., Y. Goshen-Gottstein, T. Ganel, L. J. Otten, A. Quayle, and M. D. Rugg, "Electrophysiological and haemodynamic correlates of face perception, recognition and priming," *Cerebral Cortex*, Vol. 13, pp. 739–805, 2003.

45. Jeffreys, D. A., "A face responsive potential recorded from the human scalp," *Expl. Brain Res.*, Vol. 78, pp. 193–202, 1989.

46. Bentin, S., T. Allison, A. Puce, A. Perez, and G. McCarthy, "Electrophysiological studies of face perception in humans," *Journal of Cognitive Neuroscience*, Vol. 8, pp. 551–565, 1996.

47. Rossion, B., T. Curranc, and I. Gauthier, "A defense of the subordinate-level expertise account for the n170 component," *Cognition*, Vol. 85, pp. 189–196, 2002.

48. Schendan, H. E., G. Ganis, and M. Kutas, "Neurophysiological evidence for visual perceptual categorization of words and faces within 150 ms," *Pyschophysiology*, Vol. 35, pp. 420–251, 1998.

49. Itier, R. J., and M. J. Taylor, "Source analysis of the N170 to faces and objects," *NeuroReport*, Vol. 15, pp. 1261–1265, 2004.

50. Schweinberger, S., E. Pickering, I. Jentzsch, A. Burton, and J. Kaufmann, "Event-related brain potential evidence for a response of inferior temporal cortex to familiar face repetitions," *Cogn. Brain Res.*, Vol. 14, pp. 398–409, 2002.

51. Rossion, B., C. Joyce, G. Cottrell, and M. Tarr, "Early lateralization and orientation tuning for face, word, and object processing in the visual cortex," *Cogn. Brain Res.*, Vol. 20, pp. 1609–1924, 2003.

52. Mnatsakanian, E., and I. Tarkka, "Familiar-face recognition and comparison: source analysis of scalp-recorded event-related potentials," *Clin. Neurophysiol.*, Vol. 115, pp. 880–886, 2004.

53. Friston, K. J., J. T. Ashburner, S. J. Kiebel, T. E. Nicholas, and W. D. Penny, *Statistical Parametric Mapping: The Analysis of Functional Brain Images*, London: Academic Press, 1^{st} ed., 2007.

54. Shibata, T., H. Nishijo, R. Tamura, K. Miyamoto, S. Eifuku, S. Endo, and T. Ono, "Generators of visual evoked potentials for faces and eyes in the human brain as determined by dipole localization," *Brain Topography*, Vol. 15, no. 1, pp. 51–63, 2002.

55. Huang, M., C. J. Aine, S. Supek, E. Best, D. Ranken, and E. R. Flynn, "Multi-start downhill simplex method for spatiotemporal source localization in magnetoencephalography," *Electroencephalogr. Clin. Neurophysiol.*, Vol. 108, pp. 32–44, 1998.